



**EXPERIMENTAL TESTING OF A VAN DE GRAAFF GENERATOR AS AN  
ELECTROMAGNETIC PULSE GENERATOR**

THESIS

John S. Leahy, Lieutenant Colonel, USA

AFIT-ENP-MS-16-S-075

**DEPARTMENT OF THE AIR FORCE  
AIR UNIVERSITY**

***AIR FORCE INSTITUTE OF TECHNOLOGY***

---

**Wright-Patterson Air Force Base, Ohio**

APPROVED FOR PUBLIC RELEASE; DISTRIBUTION UNLIMITED.

The views expressed in this thesis are those of the author and do not reflect the official policy or position of the United States Air Force, Department of Defense, or the United States Government. This material is declared a work of the U.S. Government and is not subject to copyright protection in the United States

AFIT-ENP-MS-16-S-075

EXPERIMENTAL TESTING OF A VAN DE GRAAFF GENERATOR AS AN  
ELECTROMAGNETIC PULSE GENERATOR

THESIS

Presented to the Faculty

Department of Engineering Physics

Graduate School of Engineering and Management

Air Force Institute of Technology

Air University

Air Education and Training Command

In Partial Fulfillment of the Requirements for the

Degree of Master of Science in Nuclear Engineering

John S. Leahy, BS

Lieutenant Colonel, USA

July 2016

DISTRIBUTION STATEMENT A.

APPROVED FOR PUBLIC RELEASE; DISTRIBUTION UNLIMITED.

AFIT-ENP-MS-16-S-075

EXPERIMENTAL TESTING OF A VAN DE GRAAFF GENERATOR AS AN  
ELECTROMAGNETIC PULSE GENERATOR

John S. Leahy, BS  
Lieutenant Colonel, USA

Committee Membership:

Dr. James C. Petrosky

Chair

Dr. William F. Bailey

Member

Dr. John W. McClory

Member

**ABSTRACT**

The purpose of this research was to evaluate an existing Van de Graaff generator facility for use as an EMP research tool. This facility's location on WPAFB may offer a unique opportunity for analysis of EMP effects and validation of electromagnetic codes, and thus is potentially of interest in its present operational format.

In order to assess the Van de Graaff, the unclassified Military Standard 464, which specifies a testing free field wave as having an intensity of 50 kV/m with a time-to-peak,  $t_{100-0}$ , of no more than 5 ns, was used as a baseline for free field analysis and this temporal standard used as a basis for generated currents. Unfortunately, the free field measurements were subject to substantial electronic interference due to electromagnetic coupling from internal wall reflections, invalidating the assessment. Therefore the primary research focus was to replicate the temporal character of the current through the Van De Graaff, which would represent the most direct coupling that could be expected from a free field wave. The research indicated a generated time-to-peak (a.k.a rise time) of 70 to 100 ns can be consistently produced, which is an order of magnitude greater than that of the Military Standard 464. The fall time is much faster than specified in Military Standard 464 due to substantial ringing in the line. Efforts were made in this research to match output to Military Standard 464 using impedance matching and capacitive decoupling. Proposed improvements to the VDG system are described in this thesis.

## **ACKNOWLEDGEMENTS**

Most importantly and above all, I thank God for having blessed me in the progress of this research and throughout my life in countless ways. I would like to acknowledge my family for their prayerful support throughout this process. I would like to thank my faculty research committee, Dr. James Petrosky, Dr. John McClory and Dr. William Bailey and most especially Dr. Gary Cook of the Air Force Research Laboratories. Dr. Cook was a very patient and encouraging mentor to me. He spent a lot of time and effort helping me with the theoretical concepts and experimental procedures.

John S Leahy

## TABLE OF CONTENTS

ABSTRACT .....	iv
ACKNOWLEDGEMENTS .....	v
TABLE OF CONTENTS.....	vi
List of Figures .....	viii
List of Tables.....	xiii
List of Variables.....	xiv
I. Introduction .....	1
Purpose.....	1
Approach .....	2
Conclusion (Review).....	4
Sponsorship .....	4
II. Theory and Assumptions .....	5
Military Standard 464.....	5
Van de Graaff, VDG, and Flash Lamp Discharge.....	6
Data Collection Sensors .....	10
CVR Operation .....	10
Highly Capacitive Circuit Elements.....	14
Circuit Impedance .....	15
Arc Diameter and Electrode Separation.....	17
Flash lamp Theory Model .....	17
VDG Theory Background .....	19
III. Methodology .....	23
Experimental Procedure .....	23
Sensors and Measurement Equipment.....	23
IV. Results and Analysis .....	26
Initial Equipment Familiarization .....	26
Non-Reproducible Waveform Improvement.....	28
D-dot Sensor Utilization.....	34
Capacitance Matching Data Collection .....	38
Reproducible Tail Pulse .....	39
Summary Comparison of Useable Data .....	47
Circuit Theory Analysis of Results .....	50
Leading Edge Data Generation Analysis .....	53

V. Discussion and Conclusions.....	66
Consistency with Flash lamp Theory .....	66
Unexpected Results .....	66
Recommendations for Future Work.....	67
Decreasing Rise Time With Additional VDGs .....	67
Equipment & Facility Improvements .....	69
APPENDIX A: Regression Performed To Fit Equations .....	71
Bibliography.....	73

## List of Figures

Figure	Page
1. The AFRLVDG during a discharge. Electrical current follows random discharge paths through the air.....	2
2. Time dependent waveforms from three sources. (Derived from Gabrielson.) .....	3
3. The Military Standard 464 EMP waveform rises to 50 kV/m. The prescribed maximum time to peak, $t_{100-0}$ , is $5.0 \times 10^{-3}$ $\mu$ s. The time to fall from peak intensity to 10% of the peak intensity, $t_{10-100}$ , is $5.9 \times 10^{-2}$ $\mu$ s. ....	6
4. Post discharge VDG illustrates Equations (2) and (3) and shows the EEMP which is the electric component of the radiant EM field. Since $i(t)$ is rapidly changing, the radiant $B(t)$ and EEMP( $t$ ) fields must also be rapidly changing. The negative charge shown on the VDG which is isolated from the ground flows to and re-combines with the positive charge shown in the ground below the strike globe.....	8
5. The CVR was used to measure $V(t)$ in the ground line after the strike globe across a constant, known resistance.....	11
6. The Prodyn model AD-40 free field D-dot sensor is constructed from two back-to-back ground plane D-dot sensors. The two $50 \Omega$ resistors, the two capacitive hemispherical areas and the flat circular ground plane are shown.....	13
7. Free field D-dot sensor area vector sensing $E_{\text{EMP}}$ field orthogonal to Poynting vector. The large circular disk is the common ground plane.....	13
8. The balun (Prodyn Model BIB-105D) on the left connects to the D-dot sensor (Prodyn Model AD-40E®) on the right.....	13
9. Toroidal Dimensions .....	14
10. Right triangle illustrating $Z$ as the vector sum of $X$ & $R$ .....	16
11. Simplified circuit representation of the experimental VDG circuit. (Paul, C., p. 182) .....	18
12. Conceptual $i(t)$ graphs correspond to the three damping classifications.....	21
13. Conceptual flash lamp current-to-resistance inverse relationship .....	22
14. CVR and D-dot experimental setup profile diagrams both shown as recording to an oscilloscope labeled #2 on the right. The signal from each of the sensing	

devices is carried from the device to the oscilloscope via an RG62 BNC cable where its waveform was temporally recorded for later analysis.....	23
15. Typical discharge waveform recorded across the CVR connected in series with the braided copper cable ground line. The $V(t)$ signal is carried to the oscilloscope on a 12" long RG62 BNC cable. Electrode separation is 9"......	26
16. Typical discharge waveform recorded across the CVR connected in series with the braided copper cable ground line. The $V(t)$ signal is carried to the oscilloscope on a 12" long RG62 BNC cable. Electrode separation is 9"......	27
17. Layout with smooth aluminum tape ground loop connected to the ground strike globe. The CVR terminals were secured in series with the ground loop. The oscilloscope remained set just outside of the metal door threshold in line with the discharge arc axis approximately 25ft from the center of the discharge arc.....	29
18. Laboratory layout with smooth aluminum tape ground loop connected to the ground strike globe which additionally highlights the extra insulation at the metal door threshold.....	30
19. Sample non-reproducible actual and fit ground line current waveform comparison are shown. The waveform corresponds to discharge #3 of Table 5. See Table 5 for additional information. .....	32
20. Discharge waveform #7 of Table 5 which followed the resumption of heavy ringing. See Table 5 for additional information.....	33
21. Comparison of the Military Standard 464 waveform with the average normalized $E_{EMP}(t)$ field based on the Table 6 average value data.....	34
22. An initial typical D-dot sensor output $V(t)$ discharge is shown. ....	35
23. The initial D-dot sensor layout includes the electrode separation distance set at 5" with the sensor set 56" orthogonally below the center of the discharge arc. ....	35
24. A typical D-dot sensor output $V(t)$ discharge is shown after applying shielding to the RG62 BNC transmission line. The electrode separation distance remains set at 5". The D-dot sensor location remains set at 56" orthogonally below the center of the discharge arc.....	36
25. A typical D-dot sensor output $V(t)$ discharge is shown after applying shielding to the RG62 BNC transmission line and moving the D-dot sensor to be 75" vertically below and 180" horizontally offset at the intersection of a laboratory wall and floor. The electrode separation distance remains set at 5". .....	37

26. The layout is shown after applying shielding to the RG62 BNC transmission line and moving the D-dot sensor to 75" vertically below and 180" horizontally offset at the intersection of the laboratory wall and floor. The D-dot sensor area vector remains orthogonal to the discharging arc .....	37
27. A sample reproducible actual and fit ground line current waveform comparison is shown. The waveform corresponds to discharge #11 of Table 8. See Table 8 notes for a description of conditions.....	42
28. Comparison of the Military Standard 464 waveform with that of the average normalized $E_{EMP}(t)$ field based on the Table 8 data.....	42
29. The CVR input and output terminals connect to the strike globe and the ground line respectively. The CVR signal is transmitted on a 25 ft shielded RG62 BNC cable. This configuration was in use while collecting the Table 8 data.....	43
30. The CVR signal is transmitted on a 25 ft shielded RG62 BNC cable and displayed on an oscilloscope. The aluminum tape visible on the floor is disconnected and cast aside. This configuration was in use while collecting the Table 8 data.....	44
31. Oscilloscope screen shot of simultaneous, D-dot and CVR voltage waveforms. The CVR generated tail pulse output is above the time axis. The D-dot sensor output is on both sides of the time axis. The waveform corresponds to discharge #11 of Table 8. See Table 8 notes for additional information. ....	45
32. A trial layout listed in Table 8 in which the D-dot sensor and CVR are used concurrently is shown. The D-dot sensor is situated 56" directly below the center of the arc. The CVR is hanging on the left side below the strike globe. The shielded RG62 BNC signal transmission lines for both collection devices are also visible.....	46
33. The average reproducible and non-reproducible experimental fit currents are shown. See Table 9 for the details pertaining to the relative magnitudes of $i_{max}$ and $t_{100-0}$ . Based on the greater $l$ and lesser $H_{abs}$ associated with the reproducible case, the reproducible case is expected to generate a greater $i_{max}$ .....	50
34. Only the independent $l$ of Equation (27) is varied to see its predicted, direct, squared effect on the dependent $t_{FWHM}$ .....	51
35. Only the independent $C$ of Equation (27) is varied to see its predicted linear, direct effect on the dependent $t_{FWHM}$ .....	52
36. Only the independent $V_o$ of Equation (27) is varied to see its predicted inverse relationship with the dependent $t_{FWHM}$ .....	52

37. The first of seven similar screen shots is shown where the CVR and D-dot sensors record simultaneously and correlate with each other for the first 40 ns. The CVR output is in yellow and is above the time axis. The D-dot output is in blue and it on both sides of the time axis.....	55
38. The first of seven similar discharge recordings is shown where the CVR and D-dot sensors record simultaneously and correlate with each other for the first 40 ns. ....	55
39. From Figure 38, the representative sample CVR discharge waveform is further isolated and is overlaid with its fit curve derived from Equation (28). The fit curve equation coefficients are found in Table 10.....	56
40. From Figure 38, the representative sample inverted D-dot discharge recording is further isolated and is overlaid with its fit curve derived from Equation (26). The fit curve equation coefficients are found in Table 10. ....	57
41. The $R^2_{D\text{-dot}} \times R^2_{CVR}$ product and the $\tau_{D\text{-dot}}/\tau_{CVR}$ ratio are optimal when equal to unity and most nearly approximate unity at 40 ns. ....	59
42. Shown graphically are the CVR and D-dot sensor fit function output levels for all seven discharges which make simultaneous use of the two sensors. These are not the maximum output values. These are the output values at 40 and 50 ns after initiating discharge.....	60
43. The average leading edge data is plotted as per the model fit to Equation (28) for both sensors from 0 to the 40 ns optimal collection duration.....	61
44. The $R^2_{D\text{-dot}} \times R^2_{CVR}$ product and the $\tau_{D\text{-dot}}/\tau_{CVR}$ ratio are optimal when equal to unity and most nearly approximate unity at 40 ns. ....	62
45. The normalized fit Equation (29) coefficient A values for both the CVR and D-dot devices are plotted together on one graph. After rounding to the nearest 10 ns the coefficient A values most closely agree at the 40 ns collection duration. ....	63
46. The normalized average graph of the leading edge output is based on data from the seven discharges where the CVR and D-dot sensors were used simultaneously. ....	64
47. The normalized average graph of the leading edge output is based on fit data from the seven discharges where the CVR and D-dot sensors were used simultaneously. The data was fit to Equation (29).....	65
48. Plan View of Improvement Concept 1.....	68
49. Plan View of Improvement Concept 2.....	69

50. To improve the model fit, the MS Excel solver tool was first selected from the data menu. Next, the  $R^2$  cell is set as the objective cell and the desired objective value is set to unity. The cells holding the constant values  $i_o$ ,  $a$ , and  $b$  of the model are selected for simultaneous processing to minimize SSE; to have  $R^2$  approach unity and to achieve optimal model fit to the actual data.....72

## List of Tables

Table	Page
1. Calculated closed form capacitance .....	15
2. Flash lamp damping classification $\alpha$ limits (Markiewicz, p. 708). ....	21
3. Equipment List .....	25
4. The first five recorded discharges were minimally oscillating, but were not reproducible. The electrode separation distance was set to 5" for all discharges.....	31
5. Extension of Table 5: The non-reproducible minimally oscillating data captured as points is further processed to a fit model current equation.....	32
6. The calculated component capacitances and measured system capacitance values are tabulated. Five minimally oscillating, but non-reproducible pulses were generated prior to making circuit improvements to $Z$ and $C$ .....	39
7. Reproducible CVR generated data with minimal ringing is tabulated. ....	41
8. Summary & comparison of observations, data, assumptions & calculations. ....	48
9. The average values of the Fit Equation (28) constants $V_o$ , $A$ and $\tau$ are shown for varying leading edge durations for both sensors. The averages are taken over all seven discharges where both sensors were used simultaneously. The analysis also shows the $\tau_{D-dot}/\tau_{CVR}$ ratio and the $R^2_{D-dot} \times R^2_{CVR}$ product for multiple durations. Also shown are each of the sample standard deviations, $\sigma$ ....	58
10. Normalized revision of Table 10 .....	62

## List of Variables

<i>A</i>	cross sectional area of current carrying path.
<i>B</i>	magnetic field
<i>C</i>	Capacitance
<i>C</i>	speed of light
<i>CVR</i>	current viewing resistor
<i>D</i>	arc route diameter
<i>D</i>	toroid diameter
<i>d</i> <sub>2</sub>	distance between the ground loop transmission and return
<i>E</i> <sub>o</sub>	energy initially stored
<i>E</i>	electric field
<i>EMP</i>	electromagnetic pulse
<i>F</i>	Frequency
<i>f</i> <sub>n</sub>	neper frequency
<i>FWHM</i>	full width half maximum
<i>H</i>	height above ground plane
<i>H</i> <sub>abs</sub>	humidity, absolute
<i>H</i> <sub>rel</sub>	humidity, relative
<i>I</i>	Current
<i>i</i> <sub>c</sub>	current, conduction
<i>i</i> <sub>d</sub>	current, displacement
<i>L</i>	Inductance
<i>L</i>	arc route length
<i>l</i> <sub>2</sub>	conductor distance traveled
<i>Q</i>	Charge
<i>R</i>	Resistance
<i>r</i> <sub>conductor</sub>	radius of the conductor
<i>R</i>	radial distance
<i>T</i>	Time
<i>t</i> <sub>FWHM</sub>	time constant, full pulse width at half amplitude
<i>t</i> <sub>100-0</sub>	time to peak
<i>V</i>	voltage or potential
<i>X</i>	Reactance
<i>Z</i>	Impedance
<i>A</i>	damping factor
<i>ε</i> <sub>o</sub>	permittivity of free space
<i>μ</i> <sub>o</sub>	permeability of free space
<i>P</i>	material resistivity

$\Omega$	radial frequency
$T$	time constant
$\Sigma$	sample standard deviations

# **EXPERIMENTAL TESTING OF A VAN DE GRAAFF GENERATOR AS AN ELECTROMAGNETIC PULSE GENERATOR**

## **I. Introduction**

### **Purpose**

One of the effects of a nuclear explosion is the production of a strong, rapidly rising electromagnetic pulse (EMP) capable of degrading the performance of critical electronic and communications systems that are integral to military hardware and war fighting functions. The EMP effects on critical systems and components must be characterized in order to protect against them. This requires testing and modeling at all system levels using consistent simulations in order to quantify the margins of uncertainty in failure analysis.

A nuclear weapon generated EMP is a result of a unique set of coupled conditions, making it relatively difficult to replicate. Therefore, establishing a generating capability that creates a reasonably close facsimile to a nuclear EMP is fundamental to support the study of EMP, and analyze models and methods for EMP hardness. This research evaluates an existing Van de Graaff generator (VDG) facility belonging to the Air Force Research Laboratories (AFRL) for its application to the study of EMP problems. The EMP free field rise time and intensity are of greatest interest. The VDG during a discharge is shown in Figure 1.

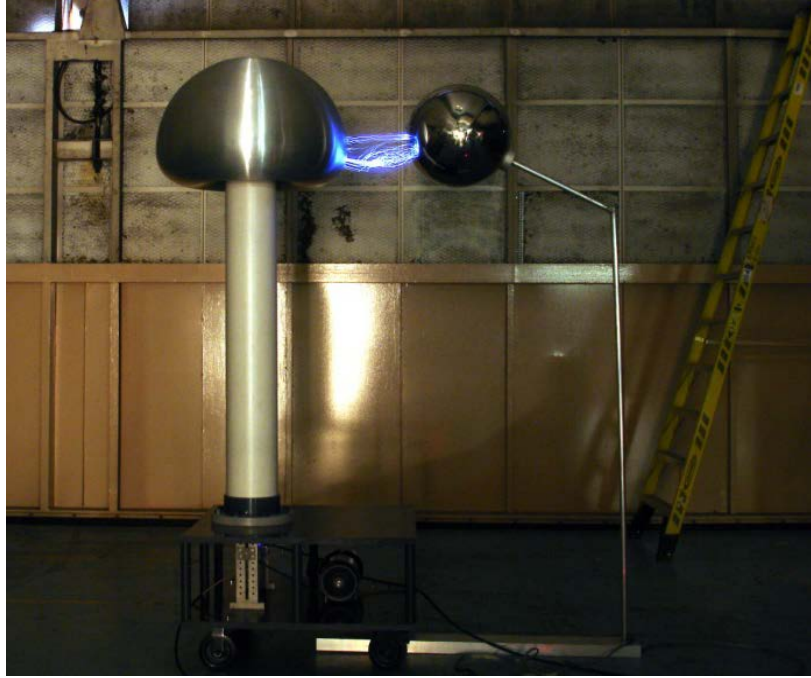


Figure 1. The AFRLVDG during a discharge. Electrical current follows random discharge paths through the air.

### Approach

A VDG generates a current pulse by mechanically moving charge from a source to an ungrounded conducting surface. The charge build-up creates a large electric field between the surface and nearby grounded objects; these act as two electrodes in a circuit. Once the breakdown field is reached, the air is ionized and current flows between the electrodes (discharge), resulting in an electromagnetic disruption. The temporal current flow can produce radiant electromagnetic fields that travel through the air and interfere with electronics. (Kodali, Chapter 2) This effect may be exploited to study the effects of EMP and to validate models associated with EM propagation. Additionally, the current flow between the electrodes during discharge can act as a source for currents replicating those resulting from a coupled EMP event. These are the overall research focus.

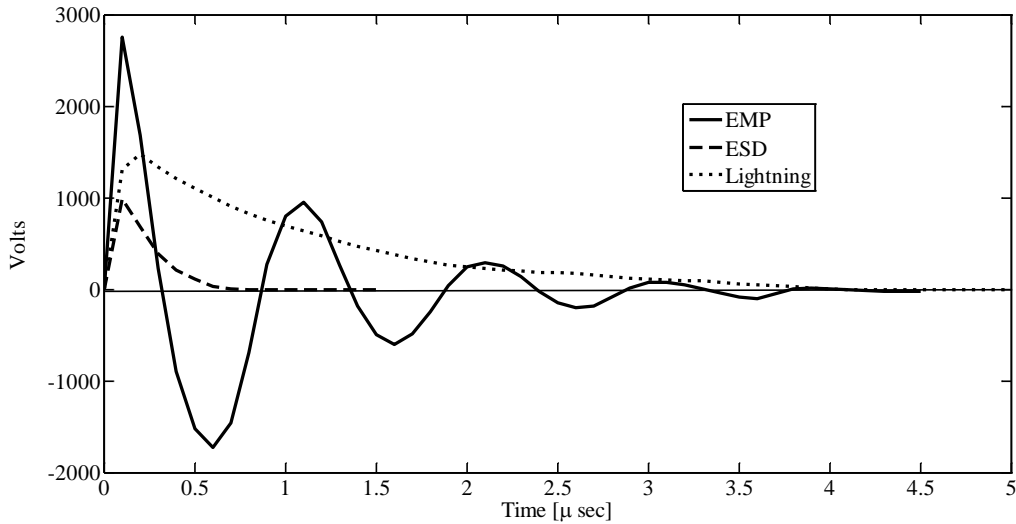


Figure 2. Time dependent waveforms from three sources. (Derived from Gabrielson.)

There were several difficulties which were overcome in this research. Initially, the free field waveform, as measured on the D-dot sensor had heavy oscillations and did not represent the desired Military Standard 464 function. The oscillations were theorized to be the result of a combination of poor impedance matching and wave reflections from laboratory surfaces. Some oscillations were removed by creating a strike plate ground electrode with a surface that matched the charging globe diameter; essentially impedance matching the VDG spark gap. The problem with the laboratory surface reflections was not able to be fully overcome. Control of the ground plate current and alterations to match the temporal characteristics of the desired EMP waveform met with more success. Current rise times for a pulse could then be controlled so as to produce reliable shots with rise times similar to those experienced from EMP.

## **Conclusion (Review)**

The primary conclusion from this research is that the current operating condition of the VDG facility cannot generate a Military Standard 464 compliant free field waveform. Proposals are offered for modifications that would increase peak electric field maximum in the pulse and reduce the rise time to the peak electric field in order to produce a waveform that may closely represent the Military Standard 464 waveform and approach suitability for validating electronic devices.

## **Sponsorship**

The research was supported through guidance and funding from the Nuclear Effects and Analysis Division, Nuclear Capabilities Directorate, Air Force Nuclear Weapons Center, Kirtland Air Force Base, New Mexico. Technical support and laboratory access were made possible by the Air Force Research Laboratory, Materials Directorate.

## II. Theory and Assumptions

### Military Standard 464

The unclassified Military Standard 464 is the test standard used for evaluation of military components that may be subject to EMP. The standard states that in the absence of other requirements, equipment designated to be EMP hard must operate through an EMP field described via a double exponential function. The double exponential function is the product of a scalar, a charging function, and a discharging function. The standard is developed, defined, and illustrated in Equation (1) and Figure 3 respectively. (Military Standard 464, March 18, 1997)

$$E(t_{sec}) = \left[ e^{-\alpha/\tau t_{sec}} - e^{-\beta/\tau t_{sec}} \right] \times E_0 [V/m] \quad (1)$$

Increasing the charging exponent,  $\beta$ , increases the rise rate and peak intensity and decreases the rise time. Increasing the discharging exponent,  $\alpha$ , significantly affects both sides of the waveform by increasing the rise and fall rate, by decreasing the rise time and fall time and by decreasing the peak intensity. Increasing the time constant,  $\tau$ , increases rise and fall times. Military Standard 464 sets nominal values of  $\alpha/\tau = 4 \times 10^7 \text{ sec}^{-1}$ ,  $\beta/\tau = 6 \times 10^8 \text{ sec}^{-1}$ , and  $E_0 = 6.5 \times 10^4 \text{ V/m}$ .

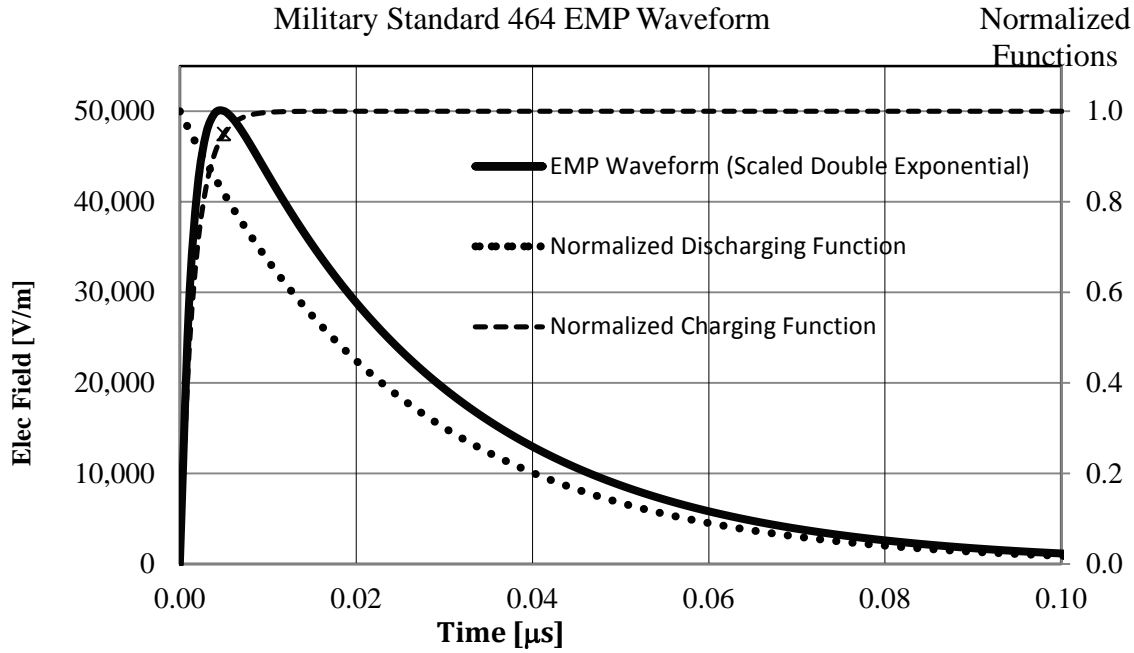


Figure 3. The Military Standard 464 EMP waveform rises to 50 kV/m. The prescribed maximum time to peak,  $t_{100-0}$ , is  $5.0 \times 10^{-3} \mu\text{s}$ . The time to fall from peak intensity to 10% of the peak intensity,  $t_{10-100}$ , is  $5.9 \times 10^{-2} \mu\text{s}$ .

### Van de Graaff, VDG, and Flash Lamp Discharge

Although not initially intended for VDG applications, flash lamp model theory was used to analyze the discharging VDG circuit. This implies that the “open air” spark (flash lamp) functions as a charge switch (Markiewicz, pp. 707-711). The VDG and flash lamp discharge systems differ in that the flash lamp discharge filament geometry is laterally constrained by a glass enclosure between two electrodes and the discharge gas is well controlled, while the VDG discharge filament geometry is only constrained by the electrodes themselves. The VDG gas is ambient air, subject to dust, humidity, and residual ionized air molecules. The borrowed theory enables predictions of how independent changes in circuit capacitance,  $C$ , electrode separation,  $l$ , and initial discharge potential,  $V_o$ , impact the system time constant,  $t_{FWHM}$ , which is directly proportional to the rise time,  $t_{100-0}$ .

During VDG charging, charge,  $q$ , is gradually delivered to the VDG and gradually builds an electric field flux and high potential along the axis between the electrodes. The electric field flux,  $\Phi_E$ , is equal to  $\oint \vec{E} \cdot d\vec{A}$ . The field flux gradually becomes sufficient to ionize the air which allows a conduction current,  $i_c$  or  $\frac{dq}{dt}$ , to pass between the electrodes.

As the electrodes are discharging, the conduction current takes on erratic paths resulting in a flux displacement and a radiant electromagnetic or *EM* field is developed as a combination of the time dependent current legs resulting from the current paths and the resultant circuit loop. While charging, the radiant *EM* field is weakly driven only by the gradually changing displacement current,  $i_d$ , which is the product of  $\epsilon_0$  and  $\frac{d}{dt} \Phi_E$ , where  $\epsilon_0$  is the permittivity of free space. The  $i_d$  exists during both the electrode charging and discharging phases because  $\Phi_E$  is changing during both phases but it does not transfer charge across the air gap during the charging phase. Once the VDG begins discharging,  $i_c$  increases from zero and  $i_d$  reverses its direction of flow such that the two current components oppose each other. Both  $i_c$  and  $i_d$  are linearly dependent on  $q$ . The  $i_d$  is linearly dependent on  $q$  because it is equal to  $\epsilon_0 \frac{d}{dt} \oint \vec{E}(t) \cdot d\vec{A}$  and  $E(t) = V(t)/l$ , where  $V(t) = q(t)/C$ . Expressed differently,  $i_d = (\epsilon_0/C) \frac{d}{dt} \oint q(t) \cdot dA$ , which has a linear dependence on  $q$ .

Electrons ionized from the air further increase  $i_c$ . The space charge left behind after ionization is reduced, but does not eliminate  $\Phi_E$ . The source driving the radiant *EM* field transitions from  $i_d$  prior to discharge to  $i_c - i_d$  post discharge. The post discharge radiant *EM* field is much greater because the rate of charge transfer is very high, i.e. time

dependence increases. The relationship between the magnetic *EM* field component,  $B$ ,  $i_d$ , and  $i_c$  follows Ampere's Law as shown in Equation (2) where  $\mu_o$  is the permeability of free space. Figure 4 illustrates Ampere's Law after discharge, where the time dependent change in  $\Phi_E$  and  $q$  contribute to  $B$ . From this a time dependent electric field is formed along with a spatially dependent magnetic field.

$$\oint \vec{B} \cdot d\vec{s} = \mu_o \left( \epsilon_o \frac{d}{dt} \Phi_E + \frac{d}{dt} q \right) \quad (2)$$

$$B(r, t) = \frac{\mu_o \{i_d(t) + i_c(t)\}}{2\pi r}$$

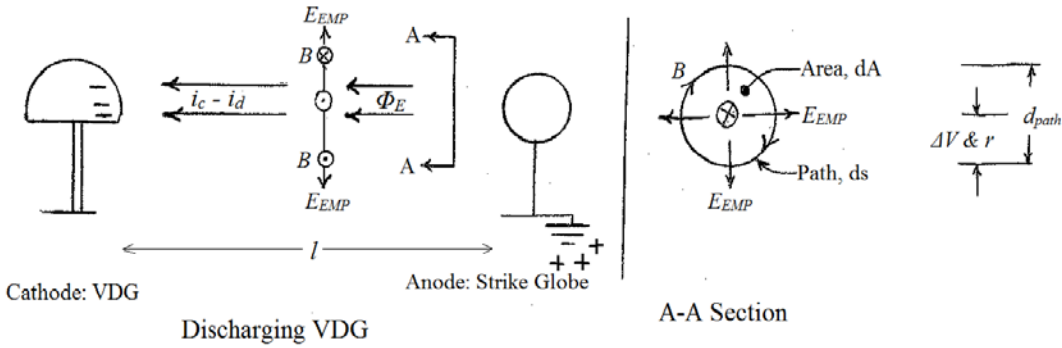


Figure 4. Post discharge VDG illustrates Equations (2) and (3) and shows the  $E$  which is the electric component of the radiant EM field. Since  $i(t)$  is rapidly changing, the radiant  $B(t)$  and  $E(t)$  fields must also be rapidly changing. The negative charge shown on the VDG which is isolated from the ground flows to and re-combines with the positive charge shown in the ground below the strike globe.

Per Faraday's law, Equation (3), as the magnetic flux changes with  $r$  and time, it generates a potential,  $\Delta V$  or  $V$ , which generates a current. Per Lenz's law, the negative sign preceding the derivative indicates that the new current is directed such as to generate a new  $B$  field to oppose the  $B$  field which created it.

$$-\frac{d\phi_B}{dt} = -\frac{d(\oint \vec{B} \cdot d\vec{s})}{dt} = -\pi r^2 \frac{d\vec{B}}{dt} = \Delta V \quad (3)$$

The term  $\Delta V$  is not the potential difference between the electrodes. This  $\Delta V$ , as shown in Figure 4, extends orthogonally from the current path to the edge of the circular

integration area,  $dA$ , and relates to the  $E$  per Equation (4) where the integration area radius,  $r$ , is as shown in Figure 4.

$$E(r, t) = \Delta V(r, t)/r \quad (4)$$

The changing  $B$  and  $E$  relate to each other through the speed of light,  $c$ , per Equation (5) since the propagation is expected to be through free space.

$$c = E/B \quad (5)$$

The  $E$  time dependence is expressed in Equation (6).

$$E(r, i(t)) = c\mu_0 \frac{i_d(t) + i_c(t)}{2\pi r} \quad (6)$$

Both  $E$  and  $B$  are changing in time due to conditions described in the next section and they are orthogonal. They eventually resolve to represent an EMP, similar to that of lightning.

Flash lamp and VDG devices are similar in that they both pulse electrical discharges through gases. Therefore flash lamp discharge theory was used in the analysis of the VDG discharge. The primary difference between the two devices is that the current filament diameter and arc length are controlled more precisely for flash lamps. The flash lamp arc length is essentially confined to the straight line distance,  $l$ , between the electrodes and the discharge gas is controlled. For the VDG, the path length,  $l + dl$ , meanders similarly to the randomness of a lightning discharge path, depending upon uncontrollable parameters such as random dust, humidity, and air paths through the laboratory.

The stochastic VDG discharge variations result in fluctuations in the arc diameter  $d$ , and the path delta,  $dl$ , and subsequently to the components of  $Z$  which will be further

described. These variations are also further manifested in changes to the electric field intensity,  $E_{max}$ , and time-to-peak,  $t_{100-0}$ . For this reason, maximizing useable data collection is especially important because it ultimately averages out the effects of the stochastic variation. The only VDG circuit variable which is directly and easily manipulated is  $l$ ; neither  $l$  nor  $d$  may be varied independently of the other. Without the ability to independently manipulate  $l$  and  $d$ , their independent effects on the waveform and on  $Z$  cannot be precisely determined. Nonetheless flash lamp theory is applied to the VDG discharge and the application will be shown to be marginally valid for predicting the VDG arc characteristics.

### **Data Collection Sensors**

Two different sensors were used for data collection. A free field D-dot sensor was initially intended to be the primary collection tool because it senses an EM wave directly. A current viewing resistor (CVR), was used to indirectly measure the current along the conductors attached to the ground electrode. It was relied upon for a majority of this research.

### **CVR Operation**

The CVR shown in Figure 5 is a small, known, constant-value resistor connected in series after the strike globe in the ground discharge cable. The  $V(t)$  across the resistor rises and falls and is recorded on the oscilloscope. From  $V(t)$  and the constant  $R$ , the  $i(t)$  is found from the Ohm's Law relationship  $i(t) = V(t)/R$ .

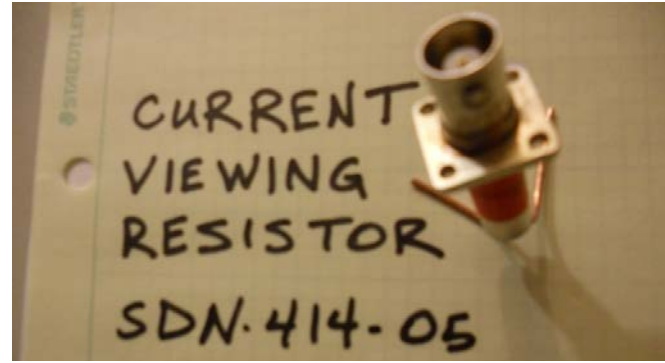


Figure 5. The CVR was used to measure  $V(t)$  in the ground line after the strike globe across a constant, known resistance.

A ground plane D-dot sensor measures the electric field time derivative by sensing the electric field flux through a known constant sensor equivalent area,  $A_{eq}$ . The “equivalent” descriptor denotes that a curved capacitive area is equivalent to a known area. The ground plane sensor transfer function outputs a voltage, derived from Gauss’s Law, Equation (7).

$$\oint \vec{E} \cdot d\vec{A} = EA_{eq} = q/\epsilon_0 \quad (7)$$

The charge,  $q$ , on the  $A_{eq}$  flows to ground through a constant known resistance. After re-arranging and taking the derivative, the ground plane sensor transfer function results in a voltage in time,  $V'(t)$ , as shown in Equation Set (8).

$$\begin{aligned}\varepsilon_0 A_{eq} \frac{dE}{dt} &= \frac{dq}{dt} = i(t) = V'(t)/R \\ V'(t) &= \varepsilon_0 \dot{E}(t) A_{eq} R = \dot{D}(t) A_{eq} R\end{aligned}\tag{8}$$

A balun equipped free field D-dot sensor combines two back-to-back ground plane D-dot sensors to form a dipole antenna. The balun combines the back-to-back ground plane sensors of equal and opposite polarity signals to output a single average voltage in time.

Specifically, the sensor and balun model used in this research were the Prodyne AD-40 and the Prodyne BIB-105D respectively. They are shown schematically and by photograph in Figure 6, Figure 7, and Figure 8. The new transfer function,  $V(t)$ , for the balun equipped free field D-dot sensor is the same as that for the ground plane D-dot sensor. The balun equipped free field sensor transfer function applied specifically to the available equipment is then as shown in Equation (9). (Edgel, "Free Field Sensors and Balun")

$$V(t) = \frac{V'(t) - (-V'(t))}{2} = \dot{D}(t) A_{eq} R = \dot{D}(t) \times 0.01 \text{ } m^2 \times 50 \text{ ohms}\tag{9}$$

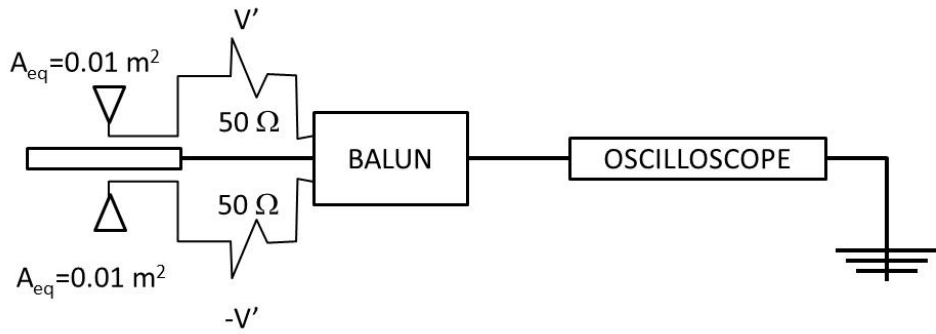


Figure 6. The Prodyn model AD-40 free field D-dot sensor is constructed from two back-to-back ground plane D-dot sensors. The two  $50\ \Omega$  resistors, the two capacitive hemispherical areas and the flat circular ground plane are shown.

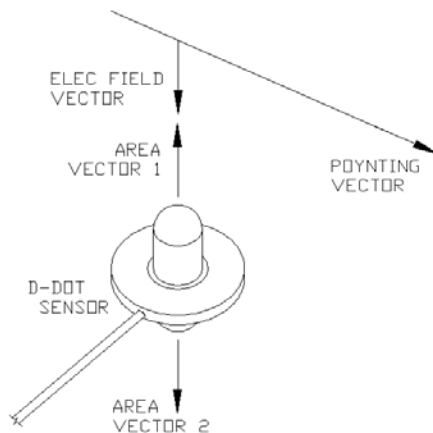


Figure 7. Free field D-dot sensor area vector sensing  $E_{EMP}$  field orthogonal to the Poynting vector. The large circular disk is the common ground plane.



Figure 8. The balun (Prodyn Model BIB-105D) on the left connects to the D-dot sensor (Prodyn Model AD-40E®) on the right.

## Highly Capacitive Circuit Elements

All circuit components of the VDG system exhibit inductance, capacitance and resistance. The VDG dome and the ground strike globe capacitance are modeled in Figure 9. The theoretical capacitance of the VDG dome was calculated as the addition of its top and bottom parts. The top part is a hollow metal hemisphere which is set over the bottom part; which is a hollow horizontally oriented half toroid. The capacitance of a hemisphere is taken as half that of a sphere and is shown in Equation (10). (Serway & Jewett, p. 724)

$$C_{hemisphere} = 2\pi\epsilon_0 r_{hemisphere} \quad (10)$$

Equation (11) is the empirical equation for the capacitance of a half-toroid,  $C_{half\_toroid}$ , in picofarads. The toroidal dimensions  $D_{Major}$  and  $D_{Minor}$  are in centimeters and are defined in Figure 9 (Johnson, Ch 2, Pg 7).

$$C_{Half-Toroid} = 0.185D_{Major} + 0.115 D_{Minor} \quad (11)$$

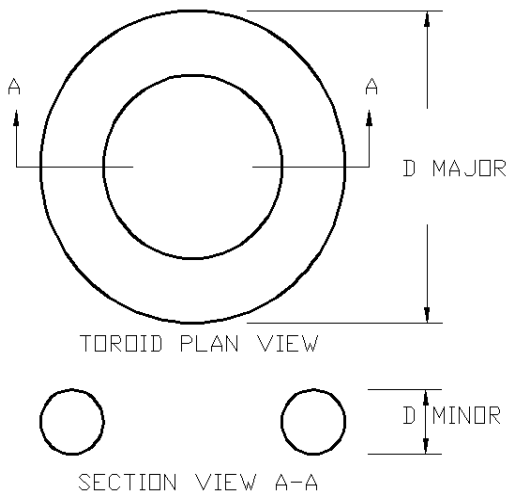


Figure 9 Toroidal Dimensions

Whereas the VDG dome is the combination of a hemisphere and a half toroid, the isolated capacitance of the VDG dome,  $C_{VDG}$ , is shown in Equation (12). The calculated capacitive values for the highly capacitive VDG dome and the ground strike globes are shown in

Table 1. The closed form calculations do not account for interactions with other structures which, if accounted for, would increase capacitance.

$$C_{VDG} = C_{half-toroid} + C_{hemisphere} \quad (12)$$

Table 1 Calculated closed form capacitance.

Calculated Capacitance, C		
VDG Dome, $C_{VDG}$	Original 17" Diam Strike Globe	Replacement 30" Diam Strike Globe
42 pF	24 pF	42 pF

### Circuit Impedance

An assumption was made that the best way to obtain usable data would be to minimize circuit impedance,  $Z$ , at every opportunity. Impedance as derived from the reactance,  $X$ , and the resistance,  $R$ , vectors is diagrammed in Figure 10 and is further expressed mathematically in Equation (13). Both  $X$  and  $R$  always oppose current. (Serway & Jewett, p. 933)

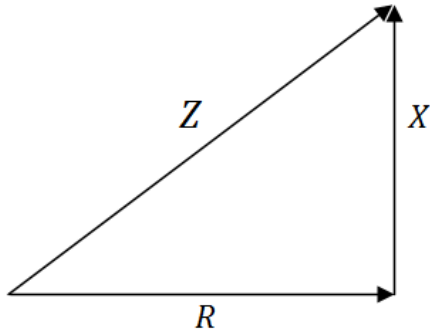


Figure 10. Right triangle illustrating  $Z$  as the vector sum of  $X$  &  $R$ .

$$Z^2 = R^2 + X^2 \quad (13)$$

The  $R$  component of  $Z$  defined in Equation (14) is the product of the material resistivity,  $\rho$ , and the distance traveled,  $l_2$ , divided by the cross sectional area,  $A$ , of the current carrying path (Serway & Jewett, p. 757).

$$R = \rho \frac{l_2}{A} \quad (14)$$

The  $X$  component of  $Z$  is mathematically defined in Equation (15) as the difference between the inductive reactance,  $X_L$  and the capacitive reactance,  $X_C$ . The inductive reactance is the product of the radial frequency,  $\omega$ , and the system inductance,  $L$ . The capacitive reactance is the inverse product of  $\omega$  and the system capacitance,  $C$ . (Serway & Jewett, pp. 928-930)

$$X = |X_L - X_C| = |\omega L - 1/\omega C| \quad (15)$$

Impedance is minimized when its  $R$  and  $X$  components are minimized. Changeable circuit dimensions and components affecting  $R$  and  $X$  included the electrode separation distance, the ground line, the strike globe, and the VDG.

### Arc Diameter and Electrode Separation

The based upon observations of many pulses, the current pulse travels between the electrodes in a random arc, as defined by a path,  $l + dl$ , along an arc with diameter  $d$ . The minimum possible path length is equal to  $l$ , the distance between the electrodes. The arc diameter is surmised to be influenced by random air impurities including dust and humidity and the current level of air ionization.

The arc diameter was observed to rise and fall with the varying current magnitude over the course of a single pulse. It is qualitatively observed to be influenced by local plasma heating and electrode separation. First, when many discharges are rapidly released, local plasma heating is observed to be sufficient to induce further ionizations which are sufficient to enable visual detection of an enlargement in  $d$ . Secondly, over the course of many VDG discharge observations,  $d$  was observed to be inversely related to  $l$ ; although it was not directly measured. In all cases,  $l$  was directly measured and recorded.

### Flash lamp Theory Model

The flash lamp model was first developed and applied in support of laser technology (Markiewicz, pp. 707-711) and will now be applied to the VDG conceptualized in Figure 11. The VDG capacitor is fully charged at  $V_o$  just prior to air breakdown which is conceptually equivalent to switch,  $S$ , closure.

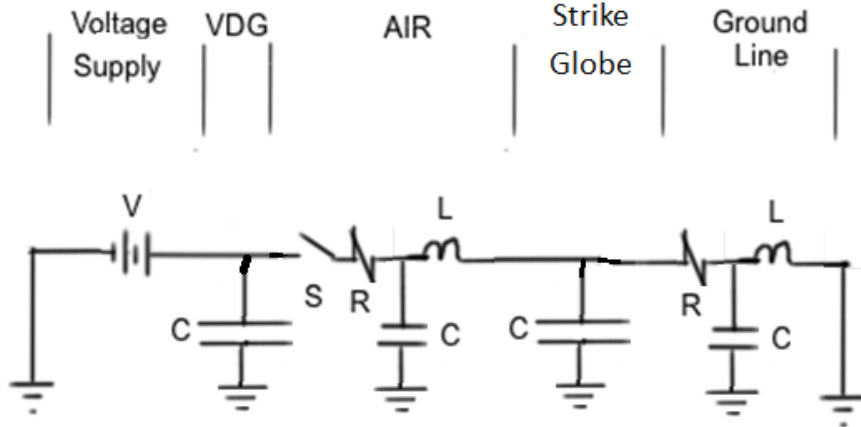


Figure 11. Simplified circuit representation of the experimental VDG circuit.  
(Paul, C., p. 182)

Flash lamp theory predicts an initially rising  $i(t)$  and  $V(t)$  and a falling  $R(t)$ . The air constant of proportionality,  $k$ , distance between electrodes,  $l$ , and arc diameter,  $d$ , are constants for a flash lamp. The theoretical  $V(t)$  and  $R(t)$  are shown in Equation Set (16).

$$R(t) = \frac{kl}{d\sqrt{i(t)}} = \frac{K_o}{\sqrt{i(t)}} \quad (16)$$

$$K_o = \frac{kl}{d}$$

Similar to other circuits, the frequency, period and damping for the VDG circuit also depend on  $C$ ,  $R$ , and  $L$ . Similarly, the maximum circuit  $V_o$  and  $E_o$  depend on assumed constants which are ultimately functions of circuit geometry, and materials.

The proportionality constants,  $K_o$ ,  $k$ , both have units of Volts-amp<sup>1/2</sup> and  $k$  depends purely on gas type and pressure without regard to any geometry. The proportionality constant is normally provided by the flash lamp manufacturer. For air at one atmosphere, such as is applicable to this research,  $k$  is arbitrarily taken as unity. Earlier research with

flash lamps found  $K_o$  experimentally by repeatedly measuring the voltage and current over many discharges.

## VDG Theory Background

Unfortunately, the VDG and flash lamp theories diverge because neither the VDG arc diameter  $d$ , and hence path length are constrained. The VDG open arc discharge makes specifying a constant  $Z$  impossible. These parameters are inter-related, such that they cannot be resolved independently and further impacting precise knowledge of  $C$ ,  $R$  and  $L$ . Furthermore the VDG arc varies stochastically from shot-to-shot even when the electrode locations remain fixed. This variability is assumed to be a result of local stochastic environmental variability in conditions including random air impurities, humidity, temperature and the current level of air ionization.

Upon VDG discharge through a gaseous medium,  $i(t)$  and  $d(t)$  initially rise to a maximum and then fall back to zero;  $R(t)$  must thus be opposite. For a flash lamp,  $d$  is necessarily bounded, but not for the VDG.

The flash lamp model differential equation with constant coefficients is shown in Equation (17). The square root term makes the differential equations non-linear. The flash lamp bore tube imposes an upper limit on the maximum arc diameter.

$$V_o(t) = L \frac{di(t)}{dt} + K_o \sqrt{i(t)} + \frac{1}{C} \int_0^t i(t) dt \quad (17)$$

Beginning with Equation (17), several steps are taken to determine whether the circuit is overdamped, critically damped, or underdamped. First, using  $V_o$  as per Equation (18),

$$1 = \frac{L(t)}{V_o} \frac{di(t)}{dt} + \frac{k}{V_o} \frac{l\sqrt{i(t)}}{d(t)} + \frac{1}{CV_o} \int_0^t i(t) dt; \quad (18)$$

substitutions are made as detailed in Equation Set (19).

$$Z_o = \sqrt{\frac{L}{C}}$$

$$i = I \frac{V_o}{Z_o}$$

$$\tau = t / t_{FWHM} \quad (19)$$

$$t_{FWHM} = \sqrt{LC}$$

$$\alpha = \frac{kl}{d\sqrt{V_o Z_o}}$$

The time constant,  $t_{FWHM}$ , is the waveform full width duration at half the maximum amplitude and  $\alpha$  is the model damping constant. The culminating flash lamp model differential equation is then as shown in Equation (20).

$$1 = \frac{dI}{d\tau} + \alpha \sqrt{I(\tau)} + \int_0^\tau I d\tau \quad (20)$$

In Equation (20), all of the variables,  $I$ ,  $\tau$  and  $\alpha$  are dimensionless. As per Equation Set (19),  $\alpha$  is an inverse function of  $\sqrt{V_o}$  where  $V_o$  corresponds to the breakdown of air. If  $V_o$  were increased,  $\alpha$  would decrease and the circuit would tend toward underdamped oscillatory ringing. Conversely, if  $V_o$  were decreased,  $\alpha$  would increase and the circuit would tend toward overdamping. Earlier research (Markiewicz, p. 708) developed the

damping classification limits in Table 2 using numerical methods. A conceptual waveform associated with each classification is illustrated in Figure 12.

Table 2. Flash lamp damping classification  $\alpha$  limits (Markiewicz, p. 708).

Overdamped	$2.0 \leq \alpha \leq 3.$
Critically Damped	$0.8 < \alpha < 2.0$
Underdamped	$0.2 \leq \alpha \leq 0.8$

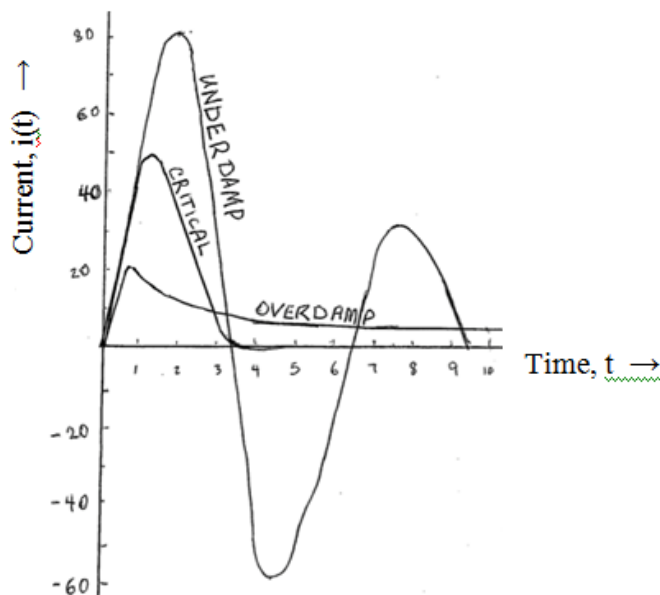


Figure 12. Conceptual  $i(t)$  graphs correspond to the three damping classifications.

Figure 13 shows a graphical, conceptual current-to-resistance inverse relationship in a flash lamp gaseous medium. Upon attaining breakdown potential, the gaseous medium ionizes; resistance falls and current rises. Both are shown to flatten out when the current diameter reaches the maximum allowable diameter as physically constrained by the bore tube.

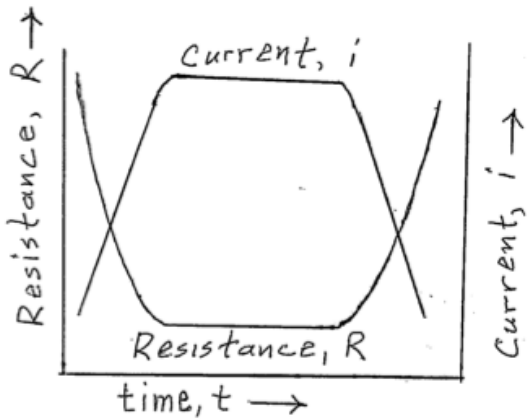


Figure 13. Conceptual flash lamp current-to-resistance inverse relationship.

Since the energy initially stored in a capacitor,  $E_o$ , is  $\frac{1}{2}CV_o^2$ , flash lamp theory and algebraic manipulations of Equation Set (19) may be used further to derive an expression for flash lamp  $C$  as shown in Equation (21). (Markiewicz, pp. 707-708) (Dishington, Hook, & Hilberg, pp. 2301-2308)

$$C = \sqrt[3]{\frac{2E_o\alpha^4t_{FWHM}^2}{K_o^4}} = \sqrt[3]{\frac{2E_o\alpha^4t_{FWHM}^2d^4}{k^4l^4}} \quad (21)$$

### III. Methodology

#### Experimental Procedure

The experimental procedure called for continuously lifting charge from ground onto the VDG to raise potential as per  $\Delta V(t) = \Delta q(t) / C$ . As the electric field between the electrodes approaches the dielectric strength of air, the oxygen and nitrogen molecules began ionizing. Once initiated, the process rapidly cascades as an avalanche and forms a plasma bridge. A rapidly rising  $i(t)$  arcs between the electrodes. The arcing emanates  $E_{EMP}(t)$  and  $B(t)$  fields outwardly. Sensors were in place to capture and record the waveform data generated from each discharge for analysis.

#### Sensors and Measurement Equipment

A conceptual illustration of each sensing instrument is shown in Figure 14. Some important details are again emphasized here.

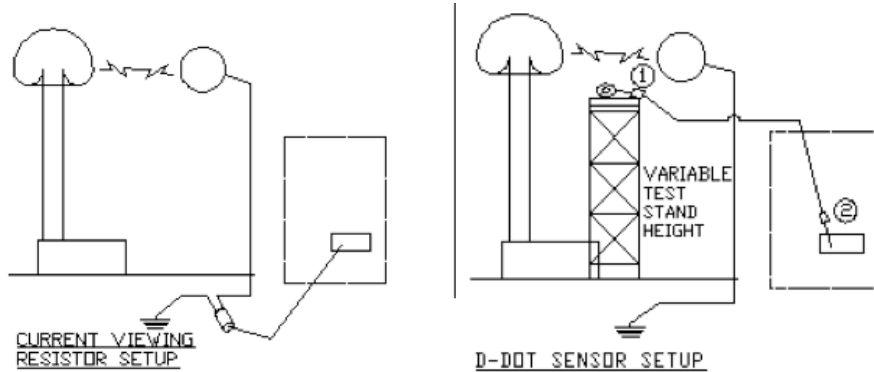


Figure 14. CVR and D-dot experimental setup profile diagrams both shown as recording to an oscilloscope labeled #2 on the right. The signal from each of the sensing devices is carried from the device to the oscilloscope via an RG62 BNC cable where its waveform was temporally recorded for later analysis.

The D-dot sensor was the initially considered the preferred data collection sensing device since it directly senses the  $E_{EMP}(t)$  field. The process calls for charge to be gradually built on the VDG until the potential between the VDG and the strike globe reaches the dielectric strength of air. With the next additional charge, the air rapidly ionizes and an  $E_{EMP}(t)$  propagates orthogonally out from the line of plasma to the D-dot sensor as illustrated in Figure 7 and Figure 14. The propagating  $E_{EMP}(t)$  field deposits charge onto the D-dot sensor which gets collected and is transmitted to ground. The results are recorded on an oscilloscope. The Results section indicates un-anticipated and interfering reflecting electromagnetic signals which were superimposed on the D-dot signal and which rendered the data un-useable.

The CVR is a device for measuring current with a known constant resistor placed in series with the ground line. It was placed as close as possible to the strike globe. Since it does not directly sense the  $E_{EMP}(t)$  through like the D-dot sensor, it is unaffected by either the direct or the reflecting EM signals. The ground line discharge voltage across the CVR was recorded at the oscilloscope and was relied upon for all consequential data collection. The  $V_{CVR}(t)$  was converted to  $i_c(t)$  via Ohm's Law and the  $i_c(t)$  was used to calculate the  $E_{EMP}(t)$  using Equation (6). The  $E_{EMP}(t)$  was fit to the standard model equation shown in (1) and compared to the Military Standard 464 waveform shown in Figure 3. Equipment used is listed in Table 3

Table 3. Equipment List

Van de Graaff Generator (VDG)	Built at AFRL
Oscilloscope	Tektronix TDS 5104B
D-dot Sensor	Prodyn AD-40E(R) SN 95
D-dot Sensor BALUN	Prodyn BIB-105D SN 132
Current Viewing Resistor 0.02487 Ω	T & M Research Products. SERIES SDN-414
Current Viewing Resistor 0.02487 Ω	T & M Research Products. SERIES SDN-414
Power Supply	No Manufacturer or Model Listed ID No.: C845588 S.N. N225035-01CJ090204
Power Switch	General Electric Fuji AF-300 Mini Model NEMA 1XCID S.N.: 7BZ471A0008
Cable	RG62A/U
Cable Terminators	93 Ω Shunt
Multimeter	Fluke 287 True RMS Multimeter
Barometer	Nimbus Digital Barometer SN B6C8F2N01
Thermometer / Humidistat	Inmac
Ground Strike Point	Improvised Equipment; 30" (0.76 m) diam foil covered stability ball.

## IV. Results and Analysis

### Initial Equipment Familiarization

As evident in Figure 15 and Figure 16 the initial waveforms were highly oscillatory, with widely ranging amplitude of ringing. None of the pulses waveforms were observed in the expected shape of a single pulse. None of these oscillatory wave forms were used in support of research conclusions.

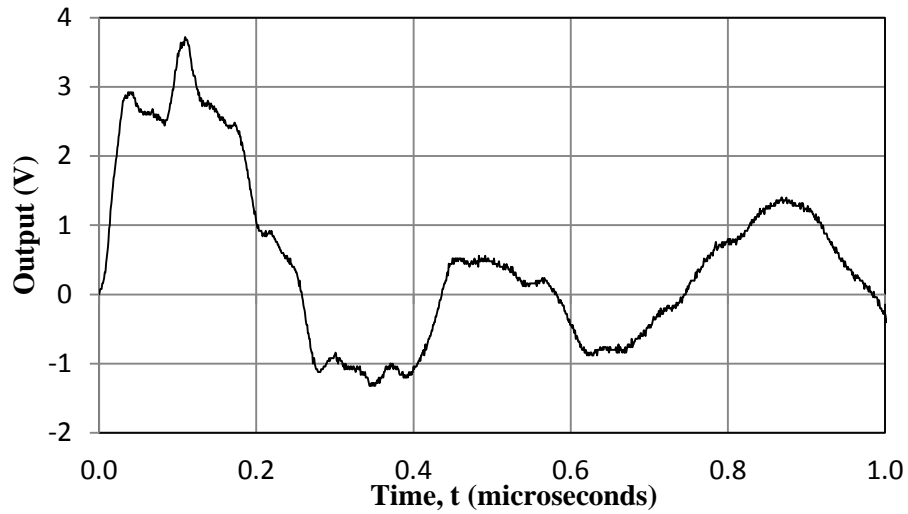


Figure 15. Typical discharge waveform recorded across the CVR connected in series with the braided copper cable ground line. The  $V(t)$  signal is carried to the oscilloscope on a 12" long RG62 BNC cable. Electrode separation is 9".

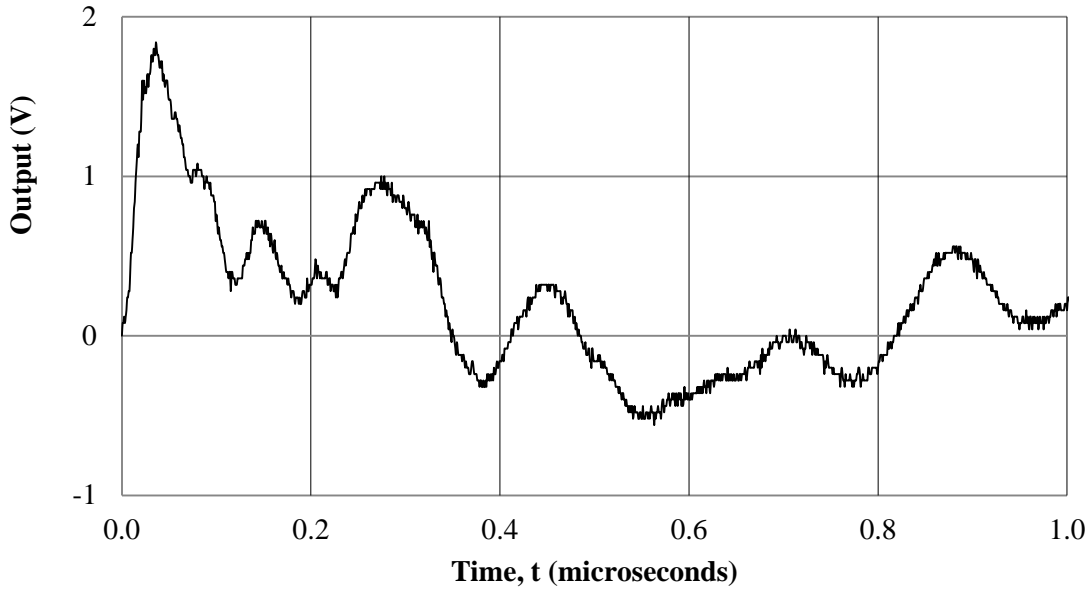


Figure 16. Typical discharge waveform recorded across the CVR connected in series with the braided copper cable ground line. The  $V(t)$  signal is carried to the oscilloscope on a 12" long RG62 BNC cable. Electrode separation is 9".

In addition to the highly oscillatory character of the waveforms, there were several other initial observations. Following each VDG discharge, the oscilloscope's keyboard and mouse were disrupted and had to be disconnected and reconnected to regain function. As evident in Figure 1, the discharge path was random. The only circuit parameter that could be controlled for each shot was the distance between electrodes,  $l$ .  $V_{max}$  varied inversely with  $l$  as did the arc diameter,  $d$ . The  $V_{max}$  was observed using an oscilloscope. The  $d$  was made initially by visually observing the arc, and approximated using equation (23).

The data collection process was paused in order to consider the issues. The ringing was speculatively theorized to be caused by radiation reflecting off the laboratory structure and/or an impedance mismatch at circuit interfaces such as that between the VDG and the

ground strike globe. The wide ranging variability in the amplitude was speculatively theorized to be caused by the continually changing local conditions in the air.

### **Non-Reproducible Waveform Improvement**

In order to reduce signal oscillations, the braided copper ground transmission loop was replaced with 1½" wide smooth aluminum tape. The tape was insulated over the floor with four thicknesses of plastic trash bags. The tape was smoother and offered greater surface area and therefore less resistance than the braided cables. The mutual inductance was minimized because the transmission and return cables are in close proximity, but the current in the two cables flow in opposite directions so that their *B* fields oppose each other. The mutual capacitance is desirably minimized in that only the tape edges (least dimension) were facing each other. The transmission loop tape is visible in the experimental layout in Figure 17.



Figure 17. Layout with smooth aluminum tape ground loop connected to the ground strike globe. The CVR terminals were secured in series with the ground loop. The oscilloscope remained set just outside of the metal door threshold in line with the discharge arc axis approximately 25 ft from the center of the discharge arc.

The first five discharges successfully generated tail pulses with very little interference or ringing. Three of the five were fully recorded and fit to the tail pulse discharge model equation,  $i(t) = i_o(e^{-\alpha t} - e^{-\beta t})$  in Table 5. Unanticipated arcing was observed penetrating the insulation where the ground loop crossed the door threshold steel. The insulation at the door threshold was therefore increased. After increasing the insulation, the arcing ended and the highly oscillatory waveforms returned. Efforts to restore conditions to generate additional data with only minimal ringing were not successful. The set up with the additional insulation over the metal threshold is shown in Figure 18.



Figure 18. Laboratory layout with smooth aluminum tape ground loop connected to the ground strike globe which additionally highlights the extra insulation at the metal door threshold.

A summary of 13 discharge events which includes 5 with minimally oscillating pulses followed by 8 with heavily oscillating pulses is shown in Table 4. Notably, the average peak-to-peak voltage for the first five minimally oscillating pulses is 5.1 V which is 38% greater than the 3.7 V average for all 13 pulses. The first five pulses subjectively take the form of a tail pulse. As an extension of Table 4, additional summary data pertaining to the three minimally oscillating pulses which were also fully recorded as points is shown in Table 5. A representative sample plot of a minimally oscillating pulse is shown in Figure 19. A representative sample plot of a later pulse after the resumption of heavy oscillations is shown in Figure 20.

Table 4. The first five recorded discharges were minimally oscillating, but were not reproducible. The electrode separation distance was set to 5" for all discharges.

11-May-11	Discharge Time	Min	Max	Peak-to-peak	Tail Pulse	Tail Pulse Point Data	Note
No.	24 Hr time	volts	volts	volts	Yes/No	Yes/No	
1	1317	-0.1	5.1	5.2	Yes	No	1
2	1321	-0.1	5.1	5.2	Yes	Yes	1,3
3	1329	-0.1	5.1	5.2	Yes	Yes	1,3
4	1330	-0.1	4.8	4.9	Yes	Yes	1,3
5	1332	-0.1	4.8	4.9	Yes	No	1
6	1353	-3.5	5.1	8.6	No	No	2
7	1420	-0.9	1.7	2.6	No	No	
8	1423	-0.7	1.3	2.0	No	No	
9	1451	-0.8	1.5	2.3	No	No	
10	1454	-0.7	1.2	1.9	No	No	
11	1459	-0.7	1.6	2.3	No	No	
12	1504	-0.5	1	1.5	No	No	2
13	1509	-0.9	3.5	4.4	No	No	
Average		-0.5	3.2	3.7			
Standard Deviation		0.4	1.8	1.5			
95% Confid.	Lower Upper	-0.7	2	2.7			
		-0.2	4.4	4.7			

Note 1: Ringing minimized.  
Note 2: Excluded highest and lowest peak-to-peak values from statistical calculations.  
Note 2: Fit data to standard equation.

Table 5. Extension of Table 4: The non-reproducible minimally oscillating data captured as points is further processed to a fit model current equation.

11-May-11	Discharge Time	Actual $i_{pk}$	Fit $i_{pk}$	Model Fit Parameters			
				$i_0$ [amp]	$\alpha$ [sec $^{-1}$ ]	$\beta$ [sec $^{-1}$ ]	$R^2$
NO:	[sec]	[amp]	[amp]				
2	1321	205.9	139.6	190.4	$2.18 \times 10^6$	$2.64 \times 10^7$	0.92
3	1329	205.9	127.2	147.5	$1.12 \times 10^6$	$3.46 \times 10^7$	0.91
4	1330	194.6	120.5	188.8	$2.83 \times 10^6$	$2.14 \times 10^7$	0.91
Average		202.1	129.1	175.6	$2.04 \times 10^6$	$2.75 \times 10^7$	0.92
Standard Deviation		6.5	9.7	24.3	$8.60 \times 10^5$	$6.63 \times 10^6$	$1 \times 10^{-2}$
95% Confid.	Lower	190.2	111.2	115.1	$4.18 \times 10^6$	$4.39 \times 10^7$	0.89
	Upper	214.1	147	236	$9.31 \times 10^4$	$1.10 \times 10^7$	0.93
MILSTD 464					$4.00 \times 10^7$	$6.00 \times 10^8$	

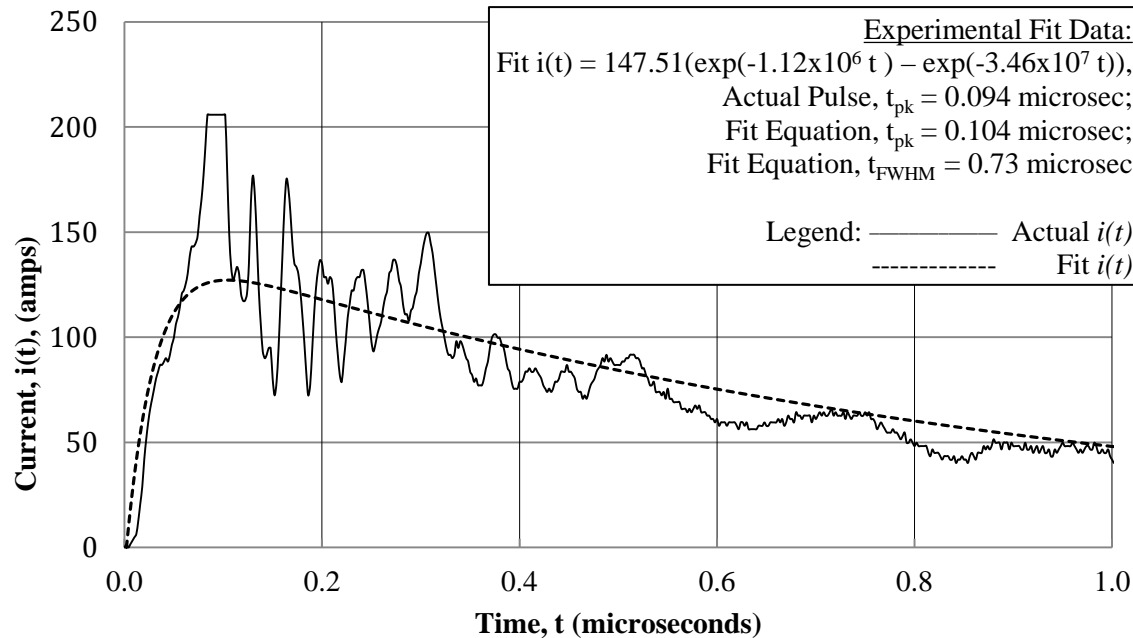


Figure 19. Sample non-reproducible actual and fit ground line current waveform comparison are shown. The waveform corresponds to discharge #3 of Table 4. See Table 4 for additional information.

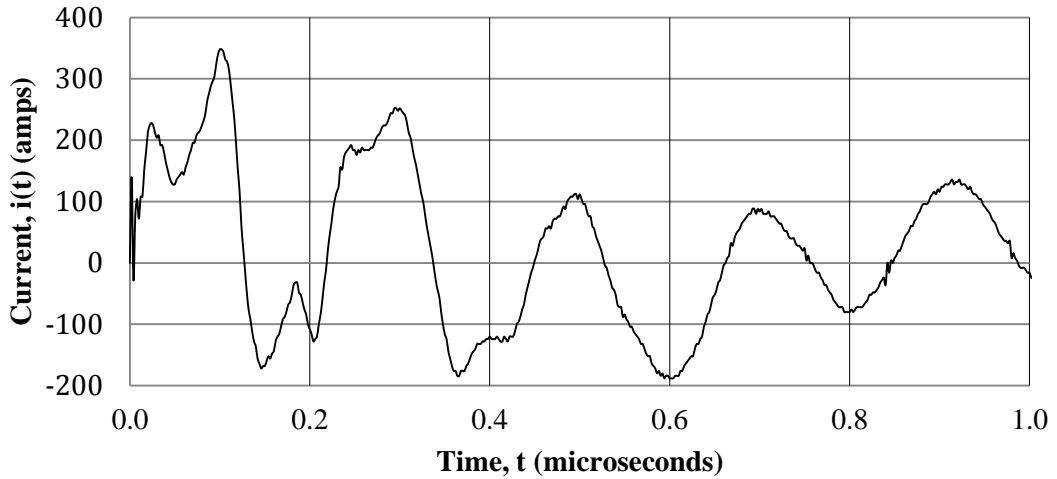


Figure 20. Discharge waveform #7 of Table 4 which followed the resumption of heavy ringing. See Table 4 for additional information.

The 50 kV/m Military Standard 464  $E_{EMP}$  requirement and the maximum ground line current are taken as inputs in the process outlined in Equation Set (22) for finding the maximum radial distance,  $r_{max}$ , from the current where the 50 kV/m intensity is attainable. The assumption of equating the current through the air to that of the ground line, will be treated later. For comparison, the normalized experimental  $E_{EMP}(r_{max},t)$  waveform is plotted together with the standard in Figure 21.

$$\begin{aligned}
 i_{ground,max}(t_{max} = 100 \text{ ns}) &= 140 \text{ A} \\
 \oint B \cdot ds = \frac{1}{c} \oint E \cdot ds &= \sqrt{\epsilon_0 \mu_0} \times E \times 2\pi r = i\mu_0 \\
 r_{max} &= \frac{i}{2\pi E} \sqrt{\frac{\mu_0}{\epsilon_0}} \quad \rightarrow \quad r_{max} = 17 \text{ cm}
 \end{aligned} \tag{22}$$

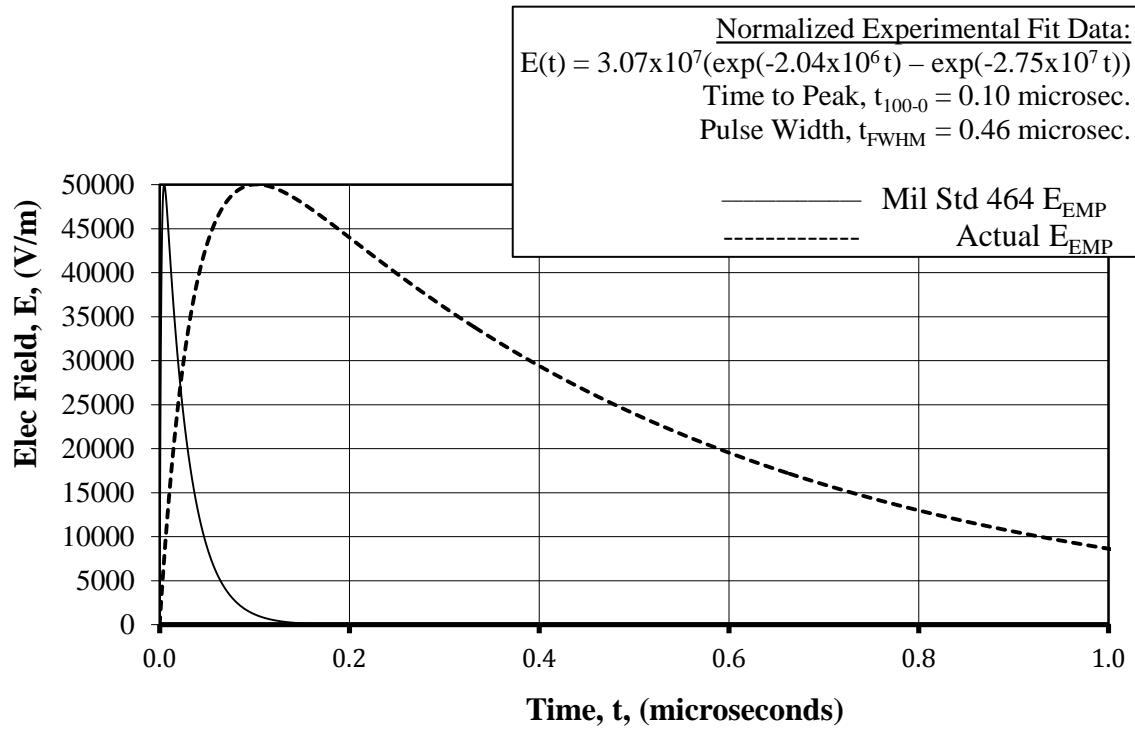


Figure 21. Comparison of the Military Standard 464 waveform with the average normalized  $E_{EMP}(t)$  field based on the Table 5 average value data.

### D-dot Sensor Utilization

Data collection with the D-dot sensor alone was attempted. All discharges recorded with the D-dot sensor exhibited a strong signal oscillation (ringing). No D-dot sensor waveform generated anything subjectively resembling a tail pulse or a tail pulse envelope. The D-dot sensor was placed 56" directly below the center of the arc and pointed straight up and orthogonally to the center of the arc. At any dimension less than 56" the VDG discharge went into the sensor rather than into the intended strike globe. Utilizing the 56" minimum dimension maximized the effect of the primary incident EMP field as opposed to the effects of reflecting and other interfering radiation. A representative sample plot is shown in Figure 22 and an initial setup with the D-dot sensor is as shown in Figure 23.

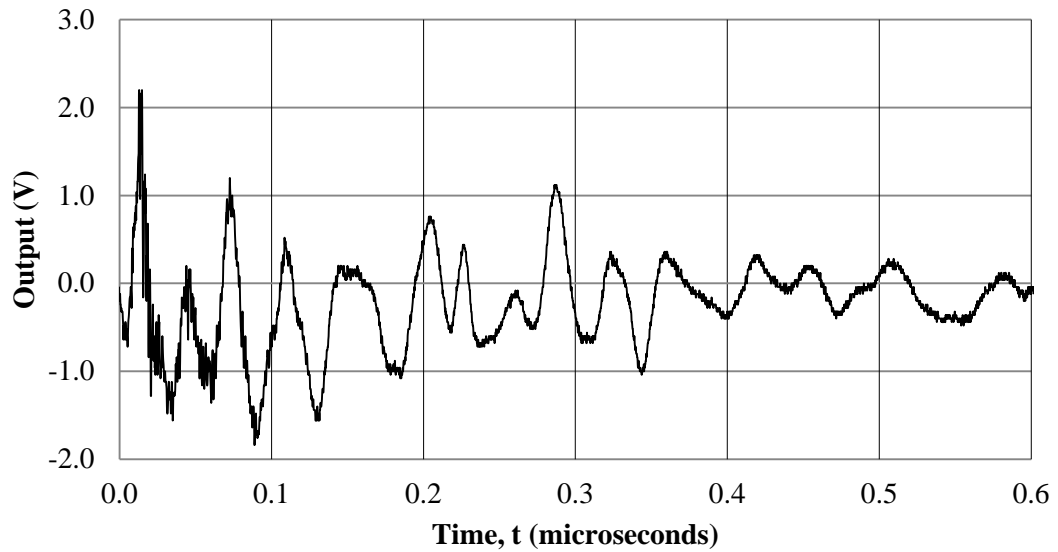


Figure 22. An initial typical D-dot sensor output  $V(t)$  discharge is shown.



Figure 23. The initial D-dot sensor layout includes the electrode separation distance set at 5" with the sensor set 56" orthogonally below the center of the discharge arc.

Two modifications were made in an effort to reduce ringing. Neither produced the desired effect. The first modification was to apply aluminum tape shielding to the RG62 BNC transmission line to the oscilloscope. A representative waveform plot is shown in

Figure 24. Without removing the line shielding, the second modification was to move the D-dot sensor 75" vertically below and 180" horizontally offset at the intersection of a laboratory wall and floor. The sensor area vector remained orthogonal to the discharge arc axis. A representative waveform plot is shown in Figure 25. A laboratory setup while using the D-dot sensor, but after implementing the two modifications is shown in Figure 26.

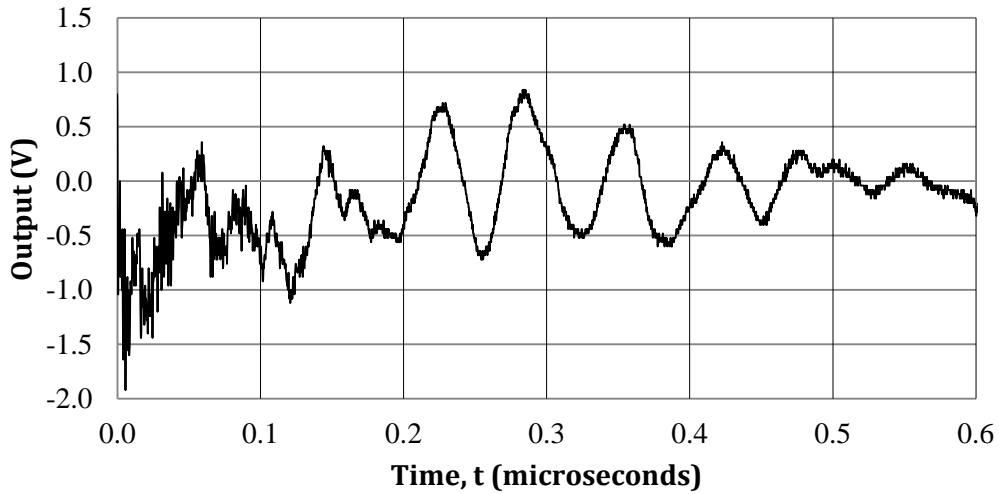


Figure 24. A typical D-dot sensor output  $V(t)$  discharge is shown after applying shielding to the RG62 BNC transmission line. The electrode separation distance remains set at 5". The D-dot sensor location remains set at 56" orthogonally below the center of the discharge arc.

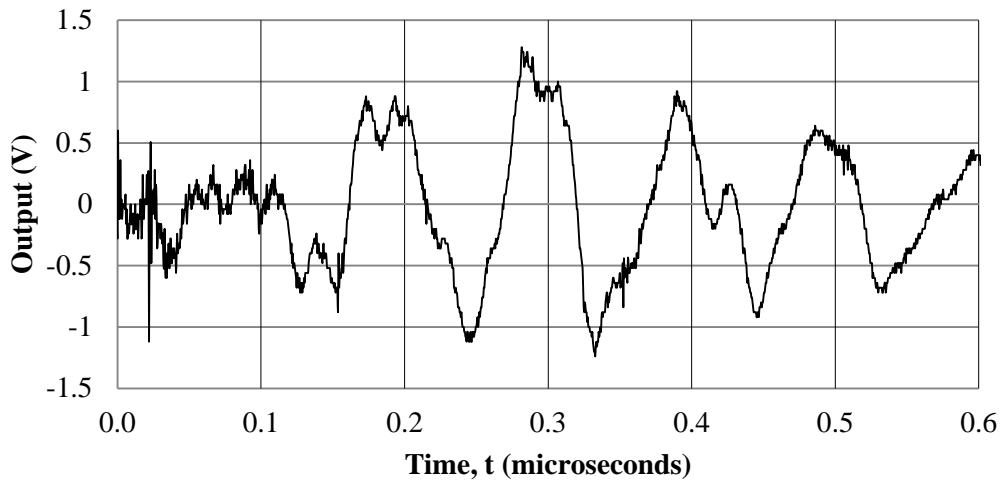


Figure 25. A typical D-dot sensor output  $V(t)$  discharge is shown after applying shielding to the RG62 BNC transmission line and moving the D-dot sensor to be 75" vertically below and 180" horizontally offset at the intersection of a laboratory wall and floor. The electrode separation distance remains set at 5".



Figure 26. The layout is shown after applying shielding to the RG62 BNC transmission line and moving the D-dot sensor to 75" vertically below and 180" horizontally offset at the intersection of the laboratory wall and floor. The D-dot sensor area vector remains orthogonal to the discharging arc.

Due to excessive interference, none of the data collected using the D-dot sensor were used in support of research conclusions.

## **Capacitance Matching Data Collection**

The next modification was to replace the 17" diameter strike globe with a 30" diameter strike globe whose capacitance in isolation was calculated to be equal to that of the VDG. The replacement strike globe was improvised from a rubber ball covered with aluminum foil.

The discharge from the VDG to the original 17" ground strike globe was modeled as though it were a fast pulsing signal carried on a cable having a small characteristic impedance connected to an electronic component having a high input impedance. In such cases, the cable pulse senses the device input impedance as its effective termination impedance. In fast pulse situations where the cable characteristic impedance is much smaller than the termination impedance, a part of the pulse signal will reverse its direction of transit and reflect back into the cable. The fast pulse reflections may be avoided by modifying the cable termination at the receiving electronic component in order to make the cable characteristic impedance nearly equal to the termination impedance. To lower a cable's termination impedance, a shunt resistor equal to the cable characteristic impedance is connected between the cable inner conductor and its outer shell. The resulting effective termination impedance is then lowered and is equal to the parallel combination of the shunt resistor and the receiving component input impedance. (Knoll, Ch 16)

As per Figure 11 and the capacitance calculations and measurements in Table 6 the VDG and the 17" strike globe are both predominantly capacitively coupled, but un-equal, circuit elements. As per Equation (13) and Equation (15), the factors which affect  $Z$  include,  $R$ ,  $C$ ,  $L$  and  $\omega$ . Therefore, the only circuit modification which stood out as being both achievable and desirable was to improve  $Z$  matching by  $C$  matching the VDG and the

ground strike globe. A multimeter was used to measure the system capacitance at the VDG of the differing experimental configurations.

Table 6. The calculated component capacitances and measured system capacitance values are tabulated. Five minimally oscillating, but non-reproducible pulses were generated prior to making circuit improvements to  $Z$  and  $C$ .

Capacitance Summary						
<u>Calculated Component Capacitance</u>			Varying Conditions; <u>Measured System Capacitance</u>			
VDG Dome, $C_{VDG}$	Original 17" Diameter Strike Globe	Replacement 30" Diameter Strike Globe	Case	Strike Globe Diam	Electrode Separation Distance, 'l'	Measured System Capacitance
pF	pF	pF				pF
42	24	42	Non-reproducible (Section 4.2)	17"	5"	436
			Reproducible (Section 4.5)	30"	15"	143

### Reproducible Tail Pulse

In addition to capacitance matching as previously described, several other circuit modifications were enacted in order to achieve the optimal configuration for generating reproducible tail pulses with greatly reduced ringing. The CVR input terminal was connected directly and immediately to the ground strike globe. The CVR output terminal was connected to a braided copper ground line cable. The CVR signal transmission cable to the oscilloscope was raised above the floor. The CVR signal was transmitted to the oscilloscope with a 25 foot shielded RG62 BNC cable and was terminated at the oscilloscope with a  $93\Omega$  shunt resistor.

The optimal configuration was in place to first generate five pulses with data collection only through the CVR. The next seven data collection discharges were

accomplished with concurrent use of both the CVR and the D-dot sensor for a total of 12 data collection discharges. All 12 collections generated through the CVR are summarized in Table 7 and Figure 28. Figure 27 shows a reproducible sample waveform together with its fit waveform. Qualitatively, none of the D-dot generated waveforms and none of the D-dot generated waveform envelopes were observed to be in the expected shape of a tail pulse.

Table 7. Reproducible CVR generated data with minimal ringing is tabulated.

16 May No.	Time	Actual $i_{\max}$ (amp)	Fit $i_{\max}$ (amp)	Electrode Separation Distance	Model Fit Eqn.: $i(t) = i_0(e^{\alpha t} - e^{\beta t})$					Note
					$i_0$ (amp)	$\alpha$ ( $\text{sec}^{-1}$ )	$\beta$ ( $\text{sec}^{-1}$ )	$R^2$		
1	1505	62.5	49.6	15"	113917	$-1.4053 \times 10^7$	$-1.4070 \times 10^7$	0.70	1	
2	1529	39	35.8	15"	113579	$-1.4056 \times 10^7$	$-1.4068 \times 10^7$	0.38	1	
3	1536	46.9	43.5	15"	113716	$-1.4054 \times 10^7$	$-1.4069 \times 10^7$	0.69	1	
4	1540	13.4	11.6	20"	113028	$-1.4060 \times 10^7$	$-1.4064 \times 10^7$	0.91	1, 3	
5	1547	20.9	20.2	10"	113079	$-1.4058 \times 10^7$	$-1.4065 \times 10^7$	0.33	1,3	
6	1728	27.5	13.7	15"	113008	$-1.4067 \times 10^7$	$-1.4072 \times 10^7$	0.66	2, 4	
7	1732	22.2	12.5	15"	113000	$-1.4071 \times 10^7$	$-1.4075 \times 10^7$	0.78	2, 4	
8	1742	18.4	12.5	15"	113001	$-1.4400 \times 10^7$	$-1.4404 \times 10^7$	0.77	2, 4	
9	1750	16.6	11.2	15"	112993	$-1.4414 \times 10^7$	$-1.4418 \times 10^7$	0.86	2, 5	
10	1755	24.7	14.1	15"	113010	$-1.4416 \times 10^7$	$-1.4421 \times 10^7$	0.71	2, 5	
11	1803	16.2	11.2	15"	112989	$-1.4435 \times 10^7$	$-1.4439 \times 10^7$	0.86	2, 6	
12	1807	22.8	13.2	15"	113001	$-1.4436 \times 10^7$	$-1.4441 \times 10^7$	0.78	2, 6	
Avg		29.7	21.7		113221	$-1.4240 \times 10^7$	$-1.4248 \times 10^7$	0.72		
Std Dev		15.2	15		365	$1.9017 \times 10^5$	$1.8689 \times 10^5$	0.14		
95% Confid Interval	Lower	18.8	11		112960	$-1.4376 \times 10^7$	$-1.4381 \times 10^7$	0.62		
Upper		40.5	32.5		113482	$-1.4104 \times 10^7$	$-1.4114 \times 10^7$	0.82		
Notes:	1	CVR recorded output; No D-dot recording								
	2	CVR and D-dot recorded output concurrently.								
	3	Excluded from table bottom summary statistics due to the difference in electrode separation distance.								
	4	D-dot sensor orthogonal displacement from arc: 7ft-2" vertically below and 7ft-0 horizontally.								
	5	D-dot sensor orthogonal displacement from arc: 4ft-8 directly below.								
	6	D-dot sensor was in line with the VDG & Strike Globe Axis & displaced 7ft-2" vertically below and 9ft-3" horizontally from the strike globe.								

Experimental & Fit Data:  
 Fit:  $i(t) = 1.13 \times 10^5 (\exp(-1.4435 \times 10^7 t) - \exp(-1.4439 \times 10^7 t))$ ,  
 Actual Pulse,  $t_{pk} = 0.066$  microsec;  
 Fit Equation,  $t_{pk} = 0.070$  microsec;  
 Fit Equation Pulse Width,  $t_{FWHM} = 0.17$  microsec

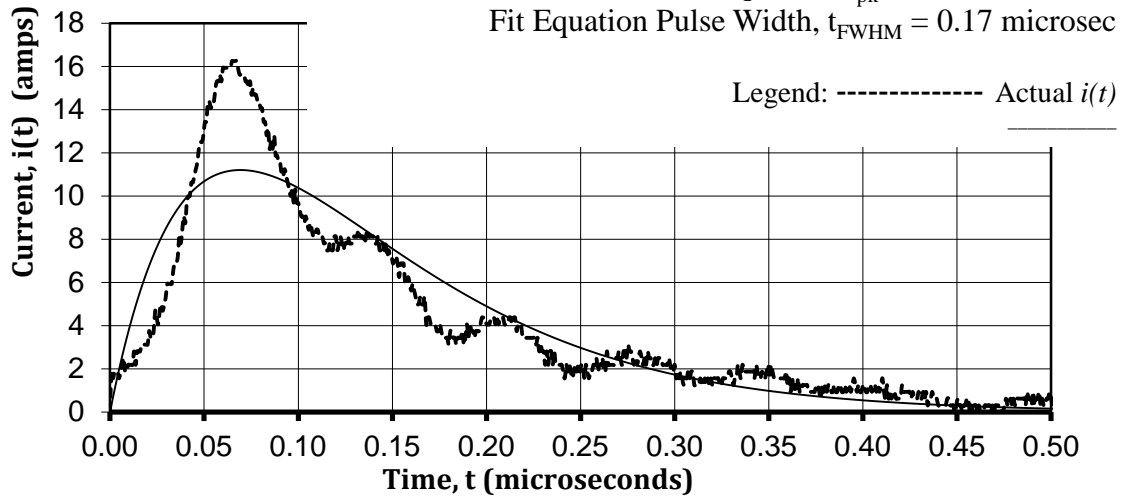


Figure 27. A sample reproducible actual and fit ground line current waveform comparison is shown. The waveform corresponds to discharge #11 of Table 7. See Table 7 notes for a description of conditions.

Average Normalized Experimental Fit Data:  
 $E(t) = 2.6237 \times 10^8 (\exp(-1.4240 \times 10^7 t) - \exp(-1.4248 \times 10^7 t))$   
 Time to Peak,  $t_{100-0} = 0.07$  microsec.  
 Pulse Width,  $t_{FWHM} = 0.17$  microsec

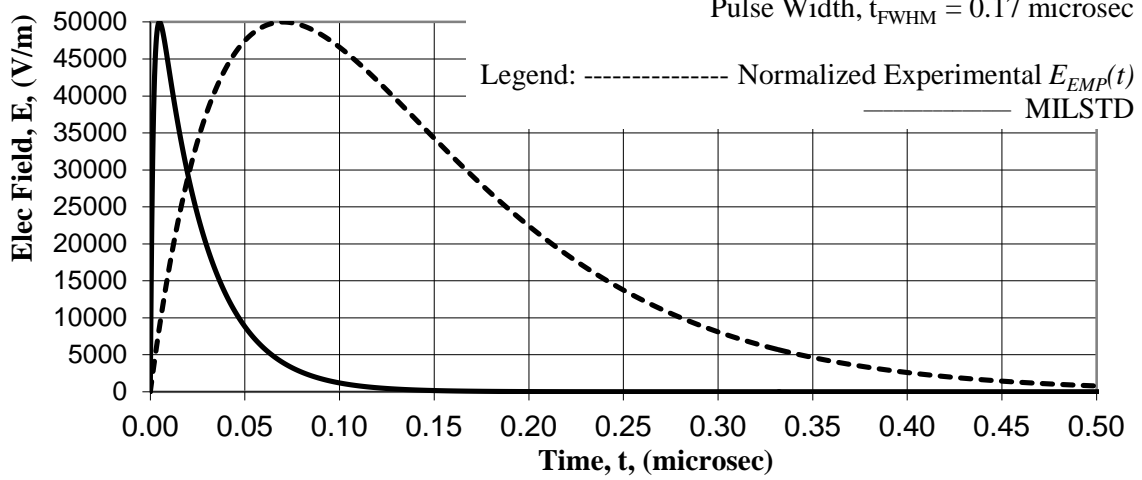


Figure 28. Comparison of the Military Standard 464 waveform with that of the average normalized  $E_{EMP}(t)$  field based on the Table 7 data.

The CVR connections near the ground strike globe are shown in Figure 29. The shielded RG62 BNC coaxial cable is highlighted in Figure 30.



Figure 29. The CVR input and output terminals connect to the strike globe and the ground line respectively. The CVR signal is transmitted on a 25 ft shielded RG62 BNC cable. This configuration was in use while collecting the Table 7 data.



Figure 30. The CVR signal is transmitted on a 25 ft shielded RG62 BNC cable and displayed on an oscilloscope. The aluminum tape visible on the floor is disconnected and cast aside. This configuration was in use while collecting the Table 7 data.

A representative sample waveform taken simultaneously through the D-dot and CVR sensors is shown as a screen shot in Figure 31. The Figure 31 CVR screen shot waveform is the same one as shown in Figure 27. Similar to the CVR signal transmission, the D-dot sensor signal transmission to the oscilloscope was also accomplished with a shielded RG62 BNC cable and it was also terminated at oscilloscope with a  $93 \Omega$  shunt resistor.

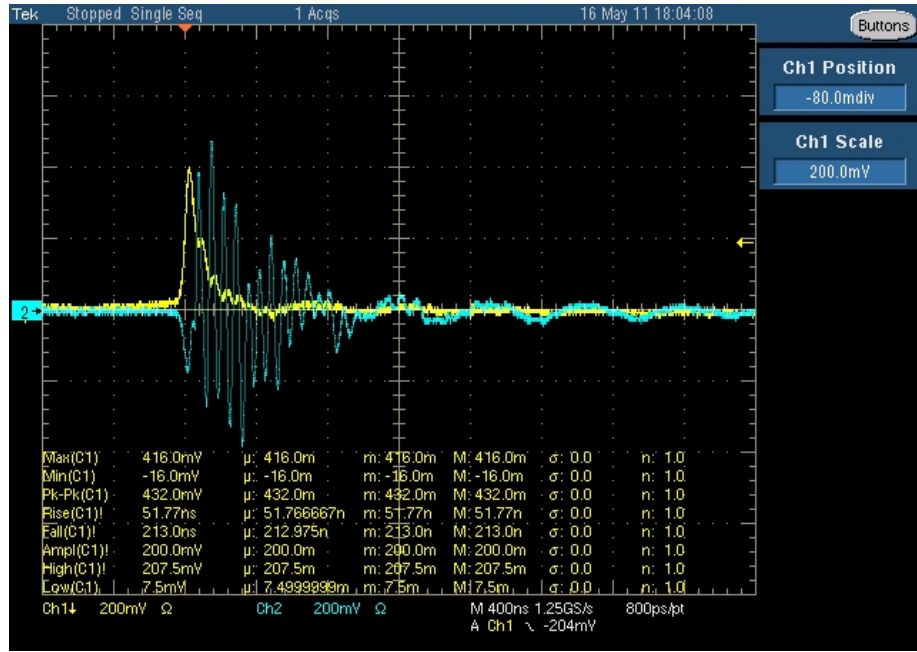


Figure 31. Oscilloscope screen shot of simultaneous, D-dot and CVR voltage waveforms. The CVR generated tail pulse output (in yellow) is above the time axis. The D-dot sensor output (in blue) is on both sides of the time axis. The waveform corresponds to discharge #11 of Table 7. See Table 7 notes for additional information.

As part of the effort to generate a smooth tail pulse without ringing, the D-dot sensor was relocated to several trial locations. Each location is described in the Table 7 notes. One of the trial locations is shown in Figure 32.

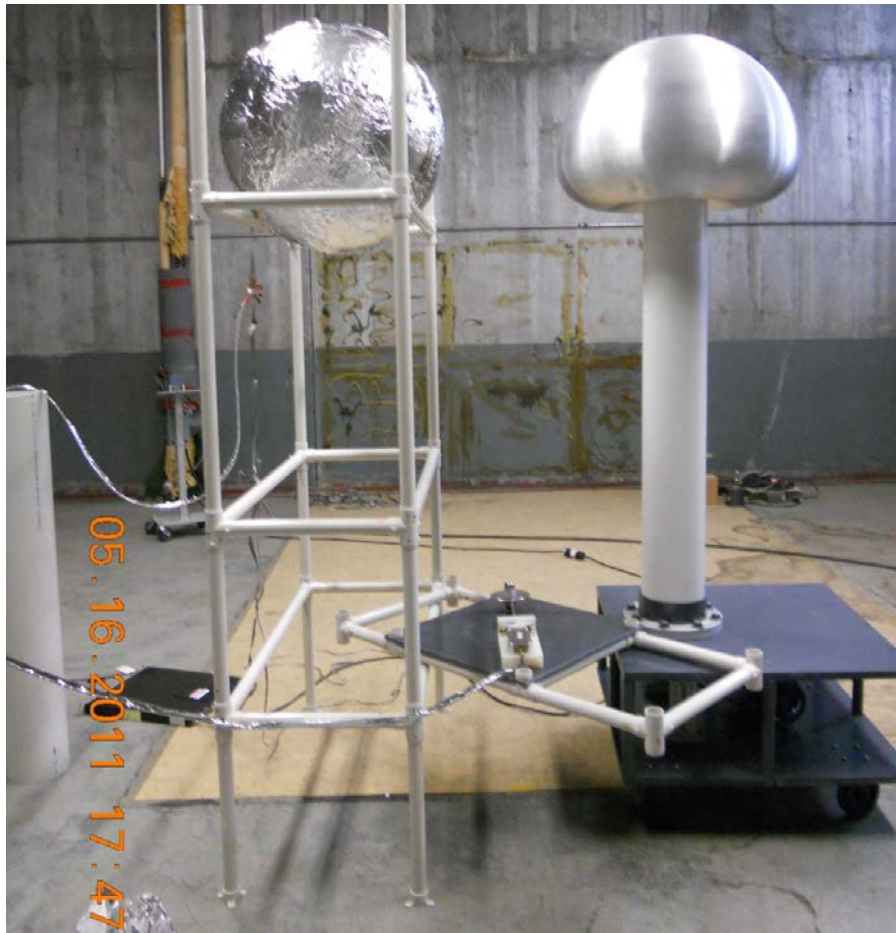


Figure 32. A trial layout listed in Table 7 in which the D-dot sensor and CVR are used concurrently is shown. The D-dot sensor is situated 56" directly below the center of the arc. The CVR is hanging on the left side below the strike globe. The shielded RG62 BNC signal transmission lines for both collection devices are also visible.

## Summary Comparison of Useable Data

The useable experimental data is summarized in Table 8. All of the useable data was generated using a known, constant  $0.02487 \Omega$  resistance CVR from which each discharge voltage was recorded as a function of time on an oscilloscope. The initial system voltage is theoretically known. The two experimental parameters that were measured independently of the arc were distance between electrodes,  $l$ , and spark gap capacitance,  $C$ . The maximum effective route diameter (assumed an arc)  $d$ , was theoretically approximated with the reproducible data as in Equation (); all parameters are listed in parameters are listed in Table 8.

$$k = 1 = \frac{K_{o,\text{non-repro}} d_{\text{non-repro}}}{l_{\text{non-repro}}} = \frac{K_{o,\text{repro}} d_{\text{repro}}}{l_{\text{repro}}} \quad (23)$$

The effective  $d$  listed in Table 8 is much smaller than that which is qualitatively observed from photographs. The observed appearance of a larger  $d$  is surmised to be due to heating of the air sufficient to induce visible radiation which expands laterally outward from the current carrying path, thereby misrepresenting  $d$ .

Table 8. Summary &amp; comparison of observations, data, assumptions &amp; calculations.

Case	No. of Discharges as Data Points	Electrode Separation Distance $l$ inches	Theoretical Break Down Potential $V_o$ kV	Temp Kelvin	Relative Humidity $H_{rel}$
Non-Reproducible	3	5	390	295.5	98%
Reproducible	10	15	1140	292.7	74%
Case	Fit Peak Conduction Current		Displacement Current $i_d = \epsilon_o (1/t_{100-0}) (V_o/l) (\pi(d_{VDG})^2/4)$		Assumed Crit Damping Factor
	$i_{c,max}$ amps		$i_d$ amps		$\alpha$ unitless
Non-Reproducible	129		123		1.4
Reproducible	22		172		1.4
Case	Assumed Flashlamp Air Constant of Proportionality	Route Diameter	Measured Rise Time (0 to 100%)	Predicted Flash Lamp Time Const OR	Measured Capacitance
	$d = kl/K_o$			Fit Pulse Width	
	$k$ Volts-amp $^{1/2}$	$d$ microns	$t_{100-0}$ nanosec	$t_{FWHM(2-1)}$ nanosec	$C$ pF
Non-Reproducible	1	4.6	100	460	436
Reproducible	1	7.3	70	172	143
Case	Flashlamp Theoretical Air Constant of Proportionality $K_o = \alpha \sqrt{(V_o t_{FWHM(2-1)} / C)}$ $K_o$ Volts-amp $^{1/2}$		Air Inductance $L_{Air} = 2l [\ln(4l/d) - 0.75] \mu_o$ $L_{Air}$ $\mu H$		Air Impedance $Z_o = \sqrt{L/C}$ $Z_o$ $\Omega$
Non-Reproducible	28398		3.6		90
Reproducible	51841		11		277

The previous experimental conditions associated with the non-reproducible data differed from the later experimental conditions associated with the reproducible data. From the experimental data,  $l$  increased by 200% while  $d$  increased by 60%. This suggests that  $d$  is relatively insensitive to the experimental conditions and the application of flash lamp theory to the VDG circuit is approximately valid over a wide range of experimental conditions.

In Figure 33 the reproducible and the non-reproducible average experimental fit  $i(t)$  pulses are compared on a single graph. The non-reproducible  $i(t)$  took only 43% more time to increase 600%. Such a result is unexpected and is not consistent with flash lamp theory including that of Equation (23). Most importantly the reproducible data generated at with  $l$  by 3 times is expected to generate the greater  $i_{max}$ . Secondly, the evidence also does not support the concept that the non-reproducible  $i(t)$  exceeds that of the reproducible  $i(t)$  because of absolute humidity,  $H_{abs}$ , effects. If all conditions were equal except that of  $H_{abs}$ , then those discharges accomplished during periods of higher  $H_{abs}$  are expected to generate a lesser  $i(t)$ , because  $H_{abs}$  contributes to charge leakage off of the VDG. According to Table 8, the reproducible discharges are accomplished in conditions of both lower relative humidity,  $H_{rel}$ , and lower temperature and therefore must necessarily also be accomplished in conditions of lower  $H_{abs}$ . Therefore, based only on  $H_{abs}$  the greater discharge is expected to correspond to the reproducible discharges. Therefore, with respect only to  $H_{abs}$  the relative  $i(t)$  result in Figure 33 is not expected.

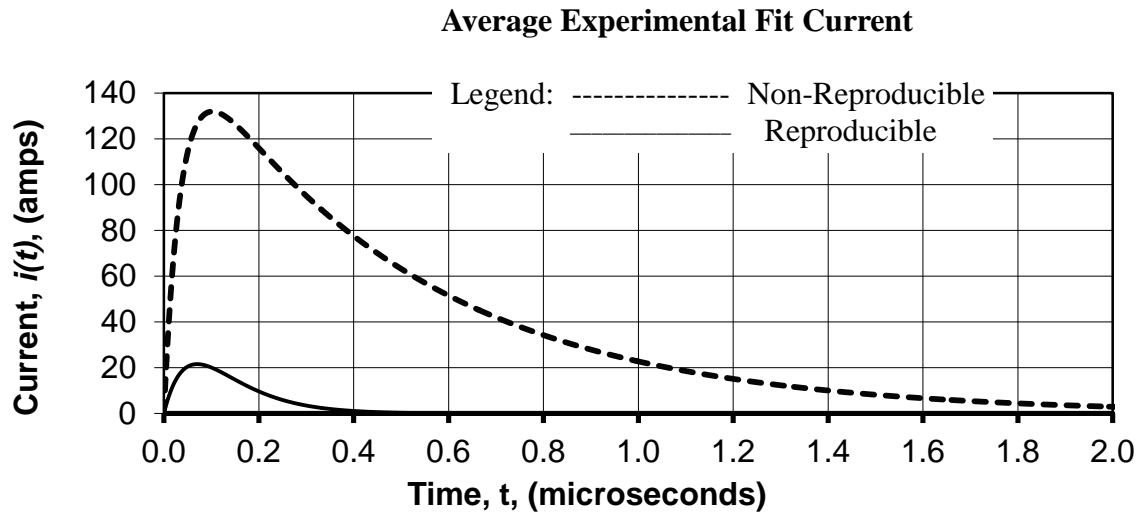


Figure 33. The average reproducible and non-reproducible experimental fit currents are shown. See Table 8 for the details pertaining to the relative magnitudes of  $i_{max}$  and  $t_{100-0}$ . Based on the greater  $l$  and lesser  $H_{abs}$  associated with the reproducible case, the reproducible case is expected to generate a greater  $i_{max}$ .

### Circuit Theory Analysis of Results

As per the measurements of this research, the existing experimental apparatus will not generate a pulse with a  $t_{100-0}$  sufficiently rapid to comply with the Military Standard 464 requirement. The standard waveform subjects test specimens to a critically over-damped electric field in which the field rises from 0 to 50,000 volts/meter in 5 ns (DOD Joint Committee, p. 59). It is, however, possible to gain insights as to how the circuit may be manipulated to more closely comply. First, Equation Set (19) shows that  $t_{FWHM(2-1)}$  equals  $\sqrt{LC}$ . With further manipulations of the experimentally measured  $t_{FWHM(2-1)}$ , and the experimentally measured  $t_{100-0}$ , another relationship is derived in Equation (24). The  $t_{100-0}$  is equal to some constant fraction,  $k_1$ , of  $t_{FWHM(2-1)}$ .

$$t_{100-0} = k_1 t_{FWHM(2-1)} \quad (24)$$

In order to better understand how to reduce the rise time,  $t_{100-0}$ , down to 5 ns, its relationship to  $k$  and  $t_{FWHM}$ , as in Equation (23), were analyzed. The  $t_{FWHM}$  may potentially be reduced by decreasing,  $l$ ; decreasing  $C$ ; or increasing  $V_o$ . The initial energy storage equation,  $E_o = \frac{CV_o^2}{2}$ , and the flash lamp capacitance equation,  $C^3 = \frac{2E_o\alpha^4 t_{FWHM}^2}{K_o^4}$ , are manipulated in order to find an expression for  $t_{FWHM}$ .

$$t_{FWHM(2-1)} = \frac{Ck^2 l^2}{V_o \alpha^2 d^2} \quad (25)$$

The assumed, average values used for plotting in Figure 34 through Figure 36 are  $C = 290 \text{ pF}$ ;  $k = 1$ ;  $l = 10''$ ;  $V_o = 765 \text{ kV}$ ;  $\alpha = 1.4$ ;  $d = 9 \mu\text{m}$ . The  $\alpha$  value falls within the critical damping range. The  $l$ ,  $C$  and  $V_o$  are varied sequentially in 34 through Figure 36 individually to better understand their impact on  $t_{FWHM}$ .

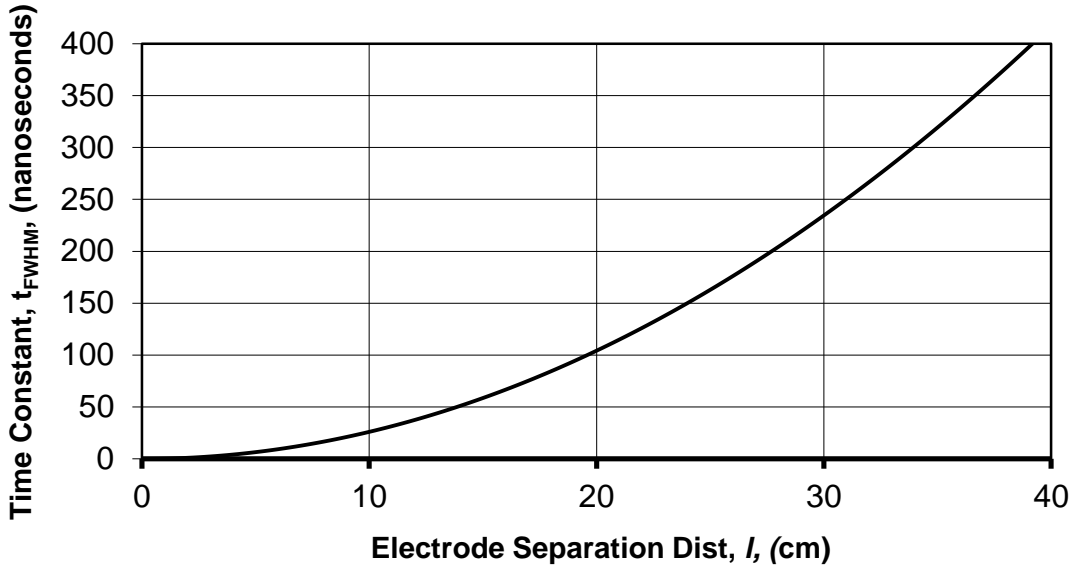


Figure 34. Only the independent  $l$  of Equation (27) is varied to see its predicted, direct, squared effect on the dependent  $t_{FWHM}$ .

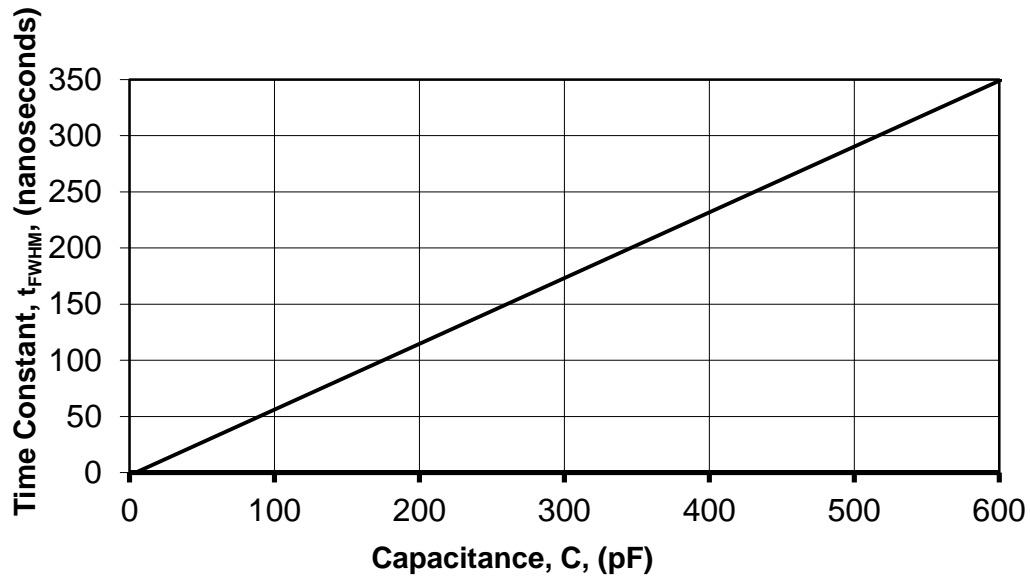


Figure 35. Only the independent  $C$  of Equation (27) is varied to see its predicted linear, direct effect on the dependent  $t_{FWHM}$ .

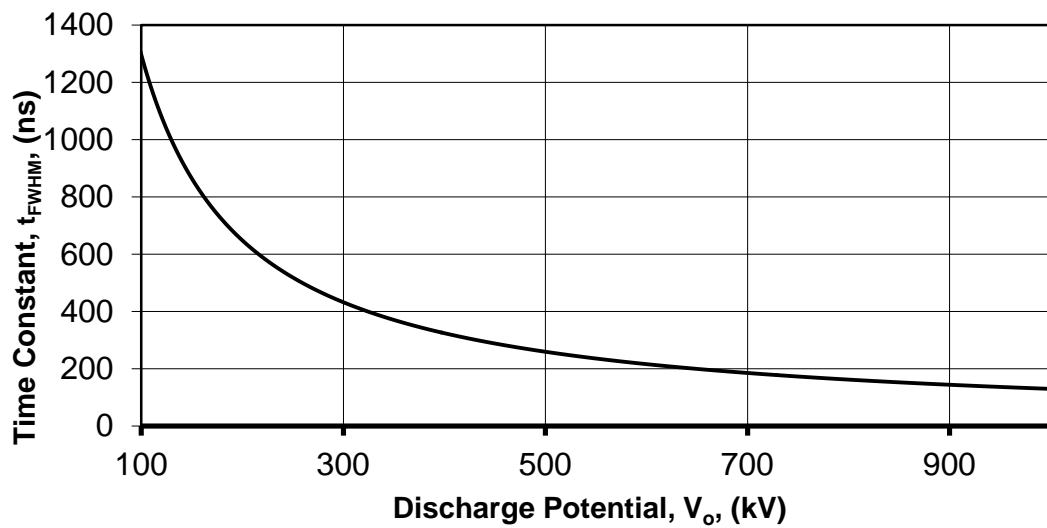


Figure 36. Only the independent  $V_o$  of Equation (27) is varied to see its predicted inverse relationship with the dependent  $t_{FWHM}$ .

## **Leading Edge Data Generation Analysis**

An analysis and comparison of the D-dot and CVR sensors were derived from the simultaneously employment of the two sensors on seven consecutive discharges. The two sensors displayed significant differences in their waveforms. As such, it is very difficult to compare the two data sets. This was further complicated by large shot to shot variation in the arcing current. In order to address this, the temporal characteristics of both sensors were analyzed over a range of timescales to identify the extent, if any, where the two sensors agreed. Speculatively, the D-dot sensor appeared to be initially measuring direct radiated field and then after approximately 40 ns appeared to superimpose re-radiated reflections from varying laboratory surfaces. As such, the D-dot generated data stream which followed the arrival of the reflections was not useable. Analysis of the D-dot generated data enabled investigators to estimate travel time and travel distances of the first reflections arriving at the sensor. An initial visual inspection of the oscilloscope screen shots over a one microsecond period did not indicate any correlation. A closer inspection indicated that the CVR and D-dot sensors strongly correlate for a short period at their leading edge. An exponential model function was assumed and fit to the leading edge data generated from both sensors. Leading edge data normalization was also analyzed to allow a direct visual comparison between the two sensors.

The leading edge data generated simultaneously via the CVR and the D-dot sensors is now modeled as a rising exponential function and analyzed. The analysis shows that the data simultaneously generated with both the CVR and D-dot sensors is nearly identical for the first 40 ns. The rest of the CVR data beyond the first 40 ns is then assumed to accurately duplicate that which would have been generated with the D-dot sensor if a

laboratory free of reflecting interference were available. This assumption is necessary since no useable D-dot data was generated for a full waveform and the D-dot sensor is what directly senses  $E_{EMP}$ .

The analysis here is derived from the last seven discharge events where data was recorded simultaneously with both a CVR and a D-dot sensor. The analysis begins by arbitrarily selecting the first of the seven discharge events as typical of all seven. The first waveform is shown both as a screen shot in Figure 37 and as a point plot in Figure 38. An initial visual inspection over a long period such as one microsecond does not indicate any correlation. Closer inspection indicates that the two sensors strongly correlate over some short period at their leading edge.

Notice in Figure 37 and in Figure 38, coincidentally, that the data begin to deviate from the initial voltage offset value 40 ns prior or to the left of where zero time was initially intended. This is the case for all of the data sets of each device. Therefore 40 ns has been added to all of the time values for all seven discharges for both sensors. This trigger location correction effectively moves all of the data to the right and re-establishes a correlated zero time location. The fact that both the trigger correction period and the correlation period are both 40 ns was not intentional.

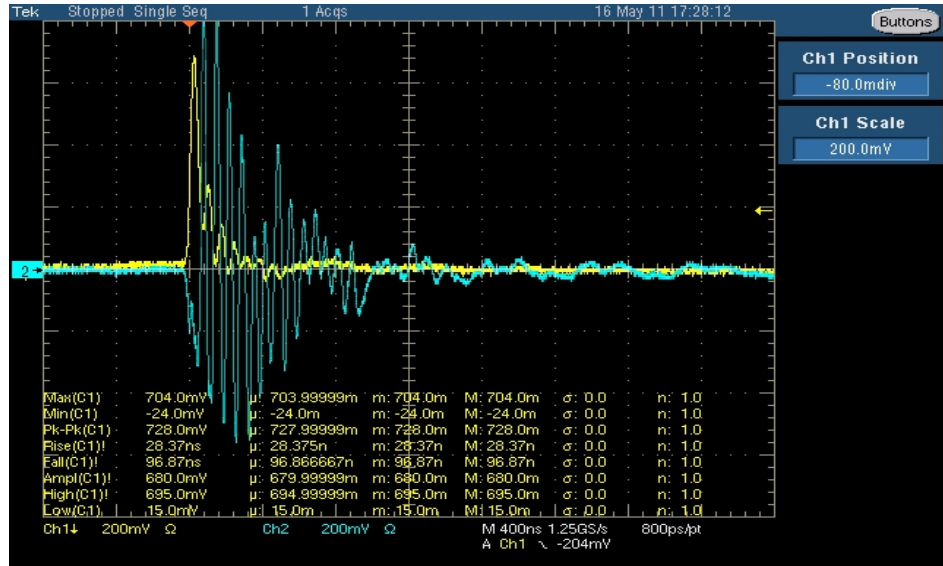


Figure 37. The first of seven similar screen shots is shown where the CVR and D-dot sensors record simultaneously and correlate with each other for the first 40 ns. The CVR output is in yellow and is above the time axis. The D-dot output is in blue and it on both sides of the time axis.

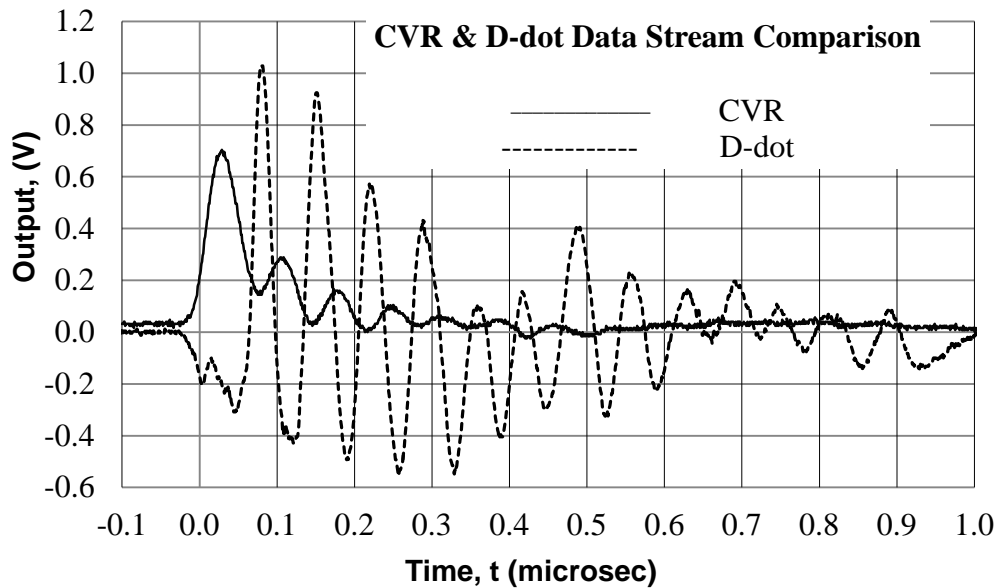


Figure 38. The first of seven similar discharge recordings is shown where the CVR and D-dot sensors record simultaneously and correlate with each other for the first 40 ns.

Figure 39 re-establishes the trigger location 40 ns to the left and isolates the leading edge CVR data from Figure 38. The overlaid CVR leading edge proposed fit equation is

shown in Equation (26). The fit equation  $V_o$  and amplitude,  $A$ , values for both devices are found in Table 9. The  $V_o$  term is included to account for the voltage offset of both sensors. The exponential term is included since the rise is assumed exponential. The ‘A’ coefficient is included to accommodate the amplitude variability and to maximize the goodness of fit.

$$V(t) = V_o + Ae^{t/\tau} \quad (26)$$

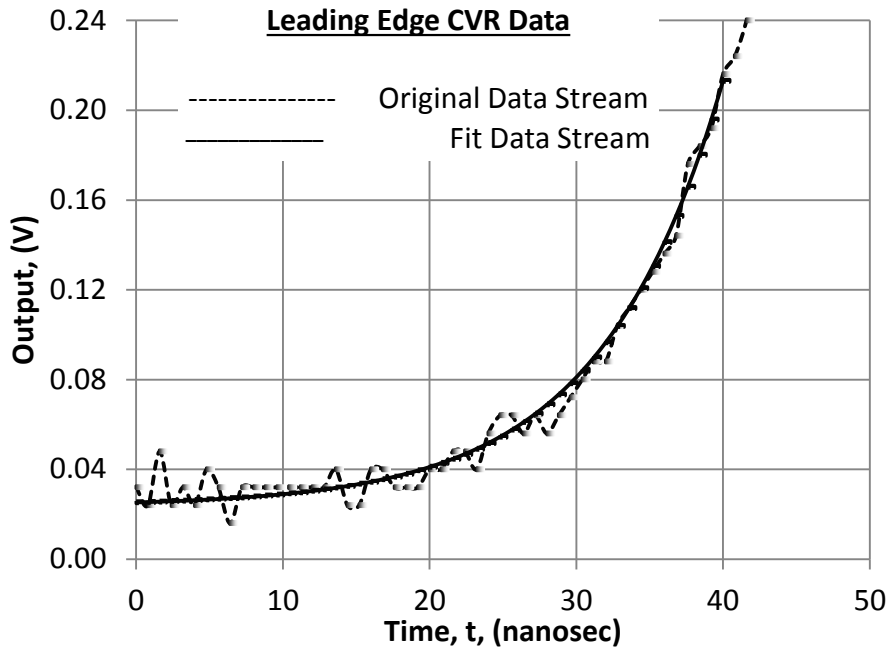


Figure 39. From Figure 38, the representative sample CVR discharge waveform is further isolated and is overlaid with its fit curve derived from Equation (28). The fit curve equation coefficients are found in Table 9.

Similarly, in Figure 40 the D-dot generated leading edge data is also further isolated and overlaid with the same initial, proposed fit equation. It is additionally inverted. The inversion was done in order to make viewing the D-dot data easier when comparing it with the CVR data.

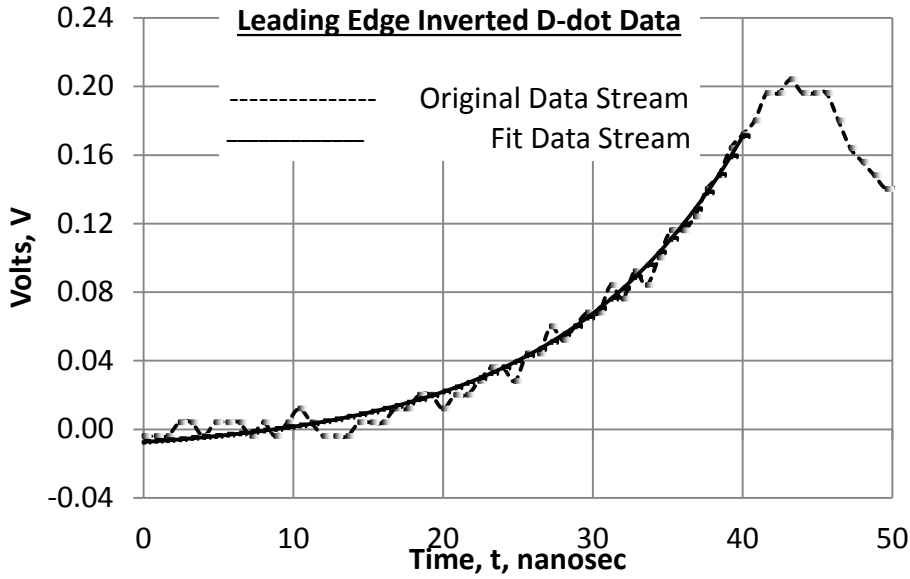


Figure 40. From Figure 38, the representative sample inverted D-dot discharge recording is further isolated and is overlaid with its fit curve derived from Equation (26). The fit curve equation coefficients are found in Table 9.

All seven discharge data sets for each sensor corresponding to the simultaneous use of both sensors were fit to the proposed Equation (28) for collection durations of 30, 40, 50 and 60 ns. For each fitting, the goodness of fit,  $R^2$ , was calculated. For each collection duration, the two average goodness of fit figures associated with each instrument were multiplied together,  $R_{CVR}^2 \times R_{D-dot}^2$ . The optimal individual goodness of fit for each device as well as the product of the two is equal to unity.

Also calculated for the four collection durations was the average  $\tau_{D-dot}/\tau_{CVR}$ . If the two instruments were perfectly matched and if there were no unequal  $V_0$  offsets to be accounted for, then the optimal  $\tau$  ratio would be exactly equal to unity. Whereas the voltage offsets are very small, the optimal  $\tau_{D-dot}/\tau_{CVR}$  ratio is still assumed to be very close to unity. The collection duration having the smallest time constant ratio standard deviation is also the most consistent.

The proposed fit to Equation (28) of the data is tabulated in Table 9 for all seven discharges for each sensor and for the 30, 40, 50 and 60 ns collection durations. The Table 9 summary shows that the optimal duration for comparing the CVR and D-dot sensor data streams is the 40 ns duration. As per Table 9 and Figure 41, the 40 ns duration is the duration at which the  $\tau_{D-dot}/\tau_{CVR}$  ratio and the  $R^2_{CVR} \times R^2_{D-dot}$  product are nearest to unity.

Table 9. The average values of the fit Equation (28) constants  $V_o$ ,  $A$  and  $\tau$  are shown for varying leading edge durations for both sensors. The averages are taken over all seven discharges where both sensors were used simultaneously. The analysis also shows the  $\tau_{D-dot}/\tau_{CVR}$  ratio and the  $R^2_{D-dot} \times R^2_{CVR}$  product for multiple durations. Also shown are each of the sample standard deviations,  $\sigma$ .

Fit Equation: $V(t) = V_o + A \times \exp(-t/\tau)$									
Fit Time	30 ns		40 ns		50 ns		60 ns		
	CVR	D-dot	CVR	D-dot	CVR	D-dot	CVR	D-dot	
Avg $V_o$	2.9E-02	-9.1E-03	7.6E-02	-5.1E-03	7.9E-02	-5.7E-04	8.8E-02	-2.5E-03	
$\sigma(V_o)$	8.5E-03	1.1E-02	1.2E-01	1.2E-02	1.1E-01	1.1E-02	1.1E-01	1.4E-02	
Avg $A$ (Volts)	8.8E-02	5.9E-03	8.0E-03	4.4E-03	8.0E-03	4.3E-03	8.0E-03	4.5E-03	
$\sigma(A)$	2.2E-01	3.2E-03	1.0E-02	1.9E-03	1.0E-02	1.9E-03	1.0E-02	1.9E-03	
Avg $\tau$ (s)	1.1E-08	1.2E-08	1.1E-08	1.1E-08	1.1E-08	1.5E-08	1.2E-08	1.4E-08	
$\sigma(\tau)$	2.7E-09	2.1E-09	2.9E-09	1.5E-09	2.9E-09	7.1E-09	3.0E-09	1.6E-09	
$\text{Avg}(\tau_{D-dot}/\tau_{CVR})$	1.12		1.03		1.28		1.15		
$\sigma(\tau_{D-dot}/\tau_{CVR})$	0.21		0.25		0.38		0.27		
Avg $R^2$	0.81		0.87		0.96		0.97		0.85
Avg: $(R^2)_{D-dot} \times (R^2)_{CVR}$	0.70		0.92		0.83		0.55		
$\sigma((R^2)_{D-dot} \times (R^2)_{CVR})$	0.19		0.06		0.10		0.21		

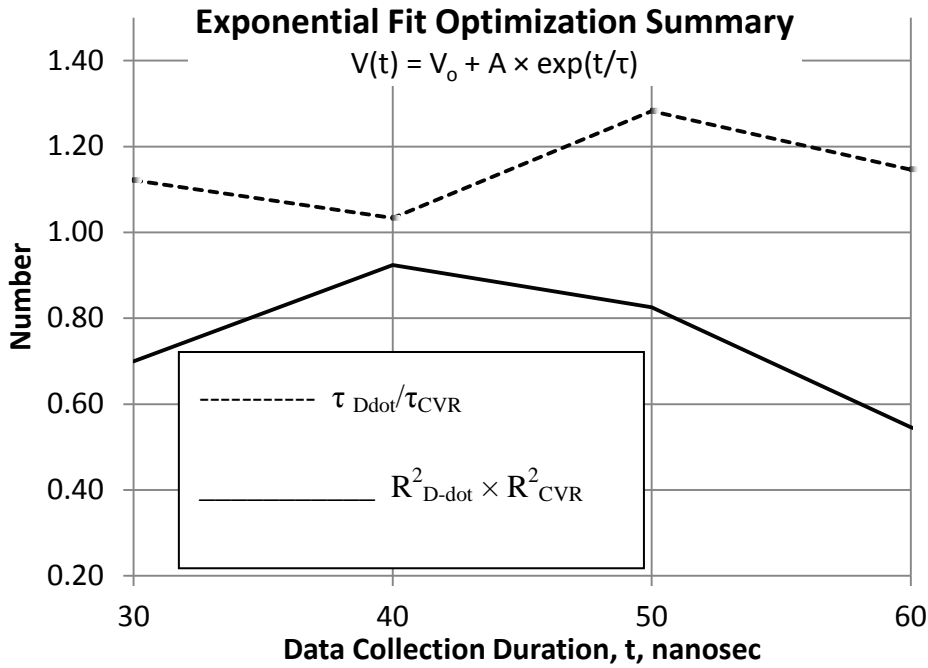


Figure 41. The  $R^2_{D\text{-dot}} \times R^2_{CVR}$  product and the  $\tau_{D\text{-dot}}/\tau_{CVR}$  ratio are optimal when equal to unity and most nearly approximate unity at 40 ns.

At or just beyond 40 ns, the D-dot sensor goodness-of-fit decreases due to assumed reflections off of laboratory surfaces. As such, the distance to the nearest reflecting surface may be estimated. The signal travels at the speed of light or approximately 1 ft/ns. The round trip travel time is taken as 40 ns which makes the distance to the nearest re-radiating surface approximately 20 feet. The actual measured distance from the arc to the nearest wall was 15 feet and the measured distance to the floor was 8 feet. However, the path of the first reflection to cause waveform interference is not known.

Beyond 50 ns, the CVR goodness of fit decreases due to the rolling over of the data and may no longer be modeled with a single exponential. Figure 42 graphically shows that for the 40 and 50 ns leading edge durations for each of the seven discharges summarized in Table 9, the CVR sensor output values exceed the D-dot sensor output values. The  $V(t)$  associated with the D-dot sensor varies directly with the arcing  $i(t)$  and inversely with the

squared orthogonal distance,  $r^2$ , from the line of the arcing  $i(t)$ . The CVR sensor  $V(t)$  values vary directly only with the ground line  $i(t)$  (i.e.:  $V(t)_{CVR} \propto i(t)$ ). Significant variability between discharge events is also observed. As previously theorized in Section 2.8, the variability is likely the result of the un-controlled environmental conditions including random air impurities, humidity, and the level of air ionization.

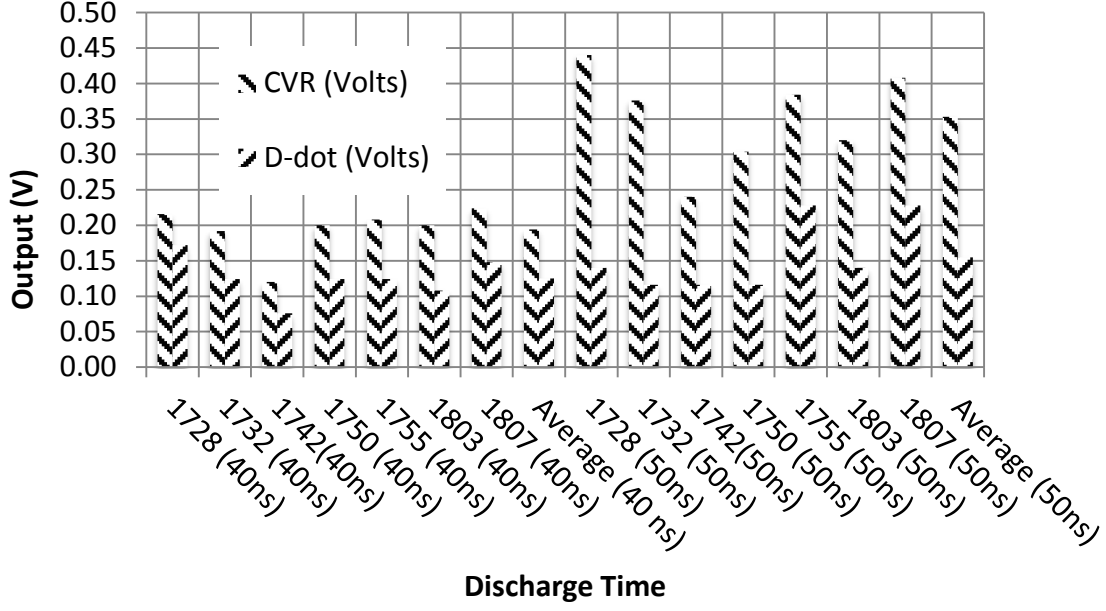


Figure 42. Shown graphically are the CVR and D-dot sensor fit function output levels for all seven discharges which make simultaneous use of the two sensors. These are not the maximum output values. These are the output values at 40 and 50 ns after initiating discharge.

In Figure 43, the average leading edge data is plotted using the model fit to Equation (28) for both sensors from 0 to the 40 ns, the optimal collection duration.

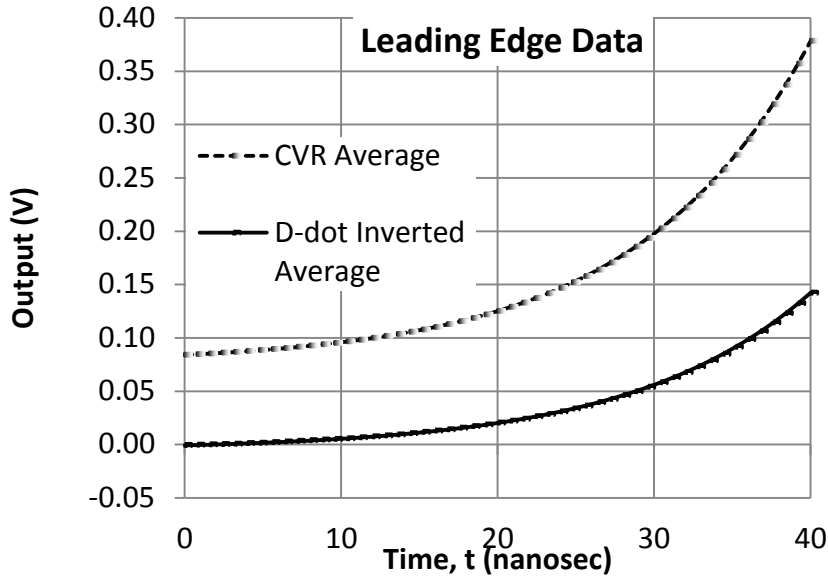


Figure 43. The average leading edge data is plotted as per the model fit to Equation (27) for both sensors from 0 to the 40 ns optimal collection duration.

Next, the data were normalized and the voltage offset,  $V_o$ , correction was eliminated. The revised data was then mapped in Figure 47 to a scale from zero to one,  $0 < V(t) \leq 1$  over 40 ns. The new model equation is as shown in Equation (27). Some small change in the  $\tau$  value was required due to eliminating the voltage offset,  $V_o$ . The revised fit equation for varying data collections durations with each collection device is shown in Table 10 and once again, as per Table 10 and Figure 44, the 40 ns duration is the duration at which the time constant ratio  $\tau_{D-dot}/\tau_{CVR}$  and the goodness-of-fit product  $R^2_{CVR} \times R^2_{D-dot}$  are nearest to unity. Dr Gary Cook assisted with specialized data processing software which was needed to adjust  $\tau$ ; compensate for eliminating  $V_o$ ; and then generate Table 10.

$$0 < V(t) = Ae^{t/\tau} \leq 1 \quad (27)$$

Table 10. Normalized revision of Table 9

Fit Time	Normalized Fit Equation: $0 < V(t) = A \times \exp(t/\tau) \leq 1$							
	30 ns		40 ns		50 ns		60 ns	
	CVR	D-dot	CVR	D-dot	CVR	D-dot	CVR	D-dot
Avg A (Volts)	6.7E-02	5.2E-02	2.5E-02	3.4E-02	2.1E-02	7.4E-02	3.3E-02	1.3E-01
$\sigma(A)$	3.2E-02	5.2E-02	1.5E-02	1.6E-02	1.2E-02	2.2E-02	1.3E-02	3.4E-02
Avg $\tau$ (s)	1.7E-08	2.7E-08	1.1E-08	1.2E-08	1.3E-08	1.8E-08	1.7E-08	2.9E-08
$\sigma(\tau)$	2.4E-08	1.7E-08	2.2E-09	1.8E-09	2.2E-09	2.5E-09	2.3E-09	5.5E-09
$\text{Avg}(\tau_{\text{D-dot}}/\tau_{\text{CVR}})$	1.61		1.06		1.42		1.73	
$\sigma(\tau_{\text{D-dot}}/\tau_{\text{CVR}})$	1.74		0.13		0.16		0.35	
Avg $R^2$	0.85	0.91	0.98	0.97	0.98	0.89	0.97	0.74
$\text{Avg}((R^2)_{\text{D-dot}} \times (R^2)_{\text{CVR}})$	0.77		0.95		0.87		0.72	
$\sigma((R^2)_{\text{D-dot}} \times (R^2)_{\text{CVR}})$	0.09		0.01		0.05		0.15	

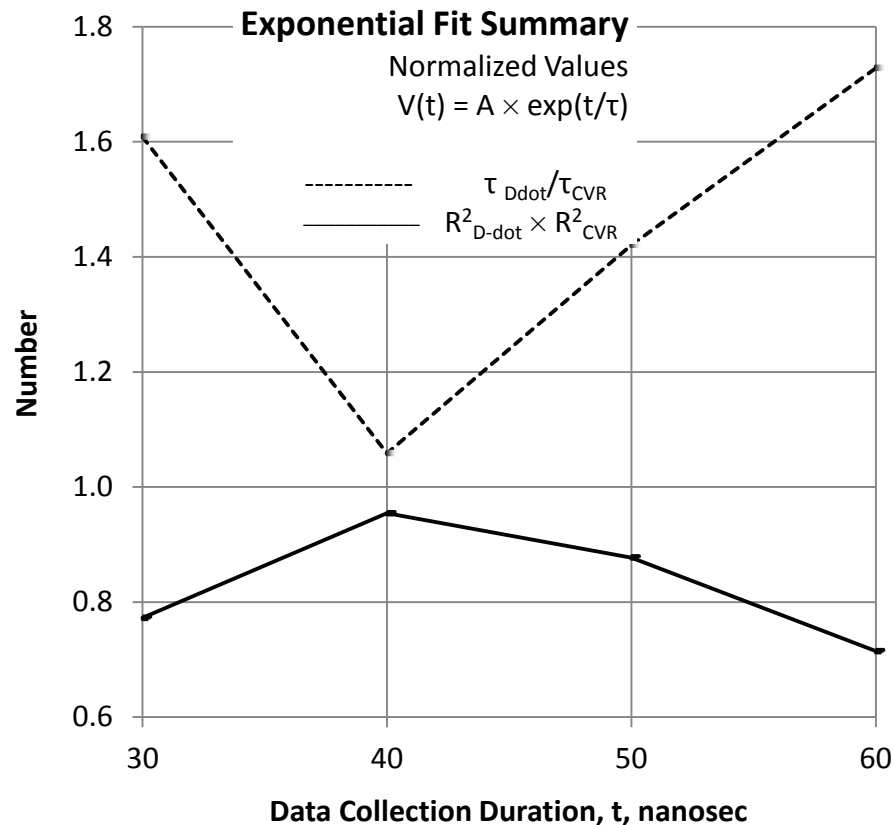


Figure 44. The  $R^2_{\text{D-dot}} \times R^2_{\text{CVR}}$  product and the  $\tau_{\text{D-dot}}/\tau_{\text{CVR}}$  ratio are optimal when equal to unity and most nearly approximate unity at 40 ns.

The Table 10  $\tau_{D-dot}/\tau_{CVR}$  ratio is nearest to unity at 40 ns which is taken as the time of maximum agreement between the two sensing devices. Similarly, the combined goodness-of-fit product is nearest to unity at 40 ns. The tabulated values at 40 ns for  $\tau_{D-dot}/\tau_{CVR}$  and  $(R^2)_{D-dot} \times (R^2)_{CVR}$  are 1.06 and 0.95 respectively. Speculatively, at greater durations, the D-dot signal experiences interference from the reflected waves which does not significantly impact the CVR generated data.

The coefficient A values for the normalized CVR and D-dot data sets are plotted in Figure 45. Once again, 40 ns was the collection duration at which the A values for the two devices most nearly agree.

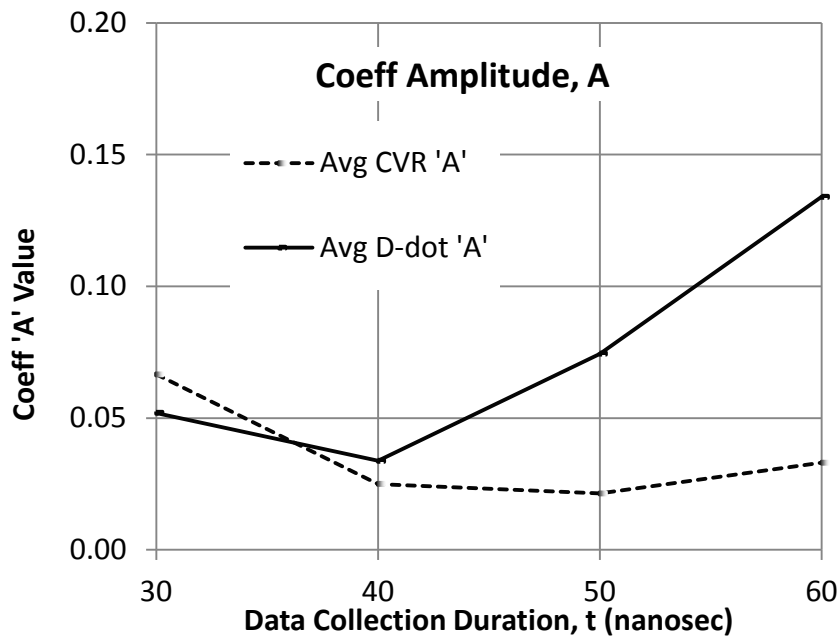


Figure 45. The normalized fit Equation (27) coefficient A values for both the CVR and D-dot devices are plotted together on one graph. After rounding to the nearest 10 ns the coefficient A values most closely agree at the 40 ns collection duration.

Figure 46 shows a 40 ns leading edge graphical comparison of the average, normalized data for both collection devices over seven discharges and is followed by Figure 47 which makes the same comparison as fit functions. The 40 ns collection duration is taken as optimal for comparing the two devices because it is at this duration where the CVR and D-dot parameter values of Equations (28) and (29) for prior to and following normalization most closely agree. Although the two leading edge curves appear similar, in order to really determine whether the two devices are conveying the same information and only scaled differently, it is also necessary to know the time-to-peak and the peak output value for both devices. In the case of the D-dot sensor, this information is not discernible due to interfering reflections.

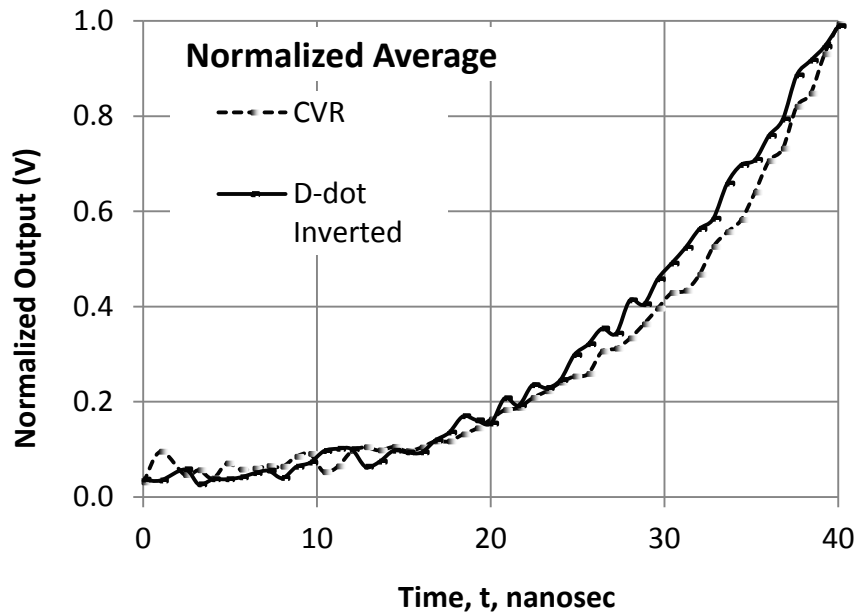


Figure 46. The normalized average graph of the leading edge output is based on data from the seven discharges where the CVR and D-dot sensors were used simultaneously.

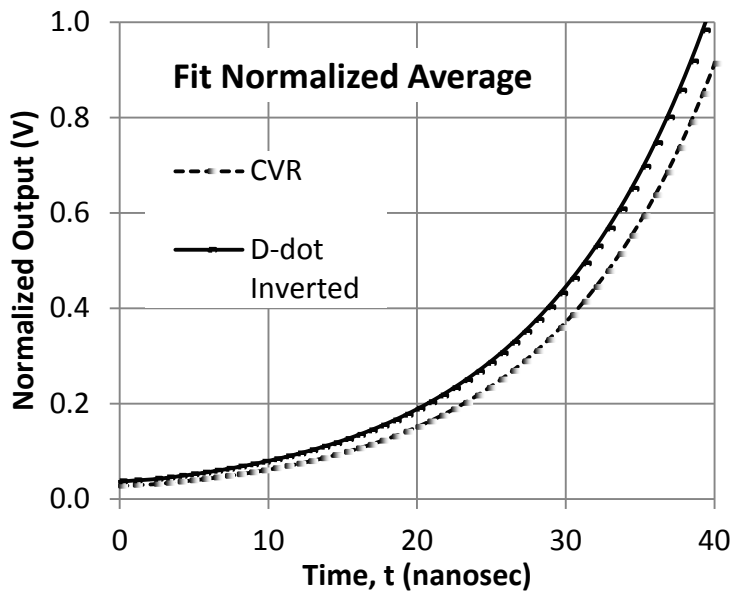


Figure 47. The normalized average graph of the leading edge output is based on fit data from the seven discharges where the CVR and D-dot sensors were used simultaneously. The data was fit to Equation (27).

## V. Discussion and Conclusions

### Consistency with Flash lamp Theory

The experimental results are generally consistent with the flash lamp theory predictions. In practice, the only way to vary the system capacitance,  $C$  and maximum charge potential,  $V_o$  is to change the electrode spacing,  $l$ . These parameters are related, through Equations (26) and (27), to the time-to peak parameter,  $t_{100-0}$ ; of direct interest in this research. The only independent parameter,  $l$ , can be precisely established and it changes  $C$  and  $V_o$ . The  $t_{100-0}$  is directly related to  $l^2$  and the system  $C$  and is inversely related  $V_o$ . Changing  $l$ ,  $C$  and  $V_o$  independently is not possible. Selecting the optimal  $l$  may be done with incremental adjustments to find the best balance to produce a waveform to most nearly comply with that of the standard, as shown in this document.

The VDG model is not entirely consistent with flash lamp theory in that  $d$  is theorized to decrease with increasing  $l$ , which was not observed. This change, however, is relatively small; the ratio of the relative change:  $\Delta d / \Delta l = -0.3$ . This suggests that  $d$  is relatively insensitive to the experimental conditions and that the application of flash lamp theory to the VDG circuit is approximately valid over a wide range of experimental conditions.

### Unexpected Results

There are a couple of unexpected & notable observations that are apparent in comparing the non-reproducible and the reproducible useable data. As per Figure 33 the non-reproducible fit  $i_{max}$  of 132 A exceeded that of the reproducible fit  $i_{max}$  of 22 A by a factor of 6. The findings show that in the non-reproducible case a 16 times greater charge quantity took 2.7 times longer to move across a shorter  $l$ . In the reproducible case,  $l=15"$

and in the non-reproducible case,  $l=5"$ . It is also unexpected & notable that the greater  $i_{max}$  was generated during a time of greater absolute humidity,  $H_{abs}$ .

There are at least two possible reasons why the conditions of a smaller  $l$  and a higher  $H_{abs}$  correspond to a larger  $i_{max}$ . First, the pre-existing dust density was neither measured nor controlled; it may have been sufficiently variable and sufficiently reduced such as to support the greater  $i_{max}$ . Secondly, the pre-existing air ionization level was neither measured nor controlled; it may have been sufficiently variable and sufficiently reduced such as to support the greater  $i_{max}$ . Neither the dust density nor the air ionization level were monitored or controlled. The air in the laboratory was not conditioned and in general the laboratory was very dusty and dirty. The exterior walls did not completely keep outside rain, dust and wind from entering the laboratory.

## **Recommendations for Future Work**

### **Decreasing Rise Time With Additional VDGs**

If a future goal is to use the VDG for research and education specifically to demonstrate theory and test models then it will be desirable to generate a faster pulse with greater intensity. It may be possible to augment the current VDG and employ it as the foundation of an improved capability. The voltage built on any single VDG is limited by both its capacitance and by the dielectric strength of air. In order to overcome existing equipment and air limitations, two concept proposals are offered. Both involve adding another VDG.

The first is as illustrated in Figure 48 as Improvement Concept 1. The two VDGs charge together in parallel at the same rate with the same polarity charge. If conditions at

VDG 1 and VDG 2 are the same except for their proximity to ground, then VDG 1 which is closer to ground will discharge first. This sudden discharge from VDG 1 to ground will result also in a large and sudden rise in potential difference possibly instantaneously exceeding the air breakdown threshold between VDG 1 and VDG 2. If such is the case then VDG 2 will discharge across a minimal gap to VDG 1. The impedance between the two VDGs is lowered as the gap distance is decreased. The anticipated and desired end result is to decrease  $t_{100-0}$ .

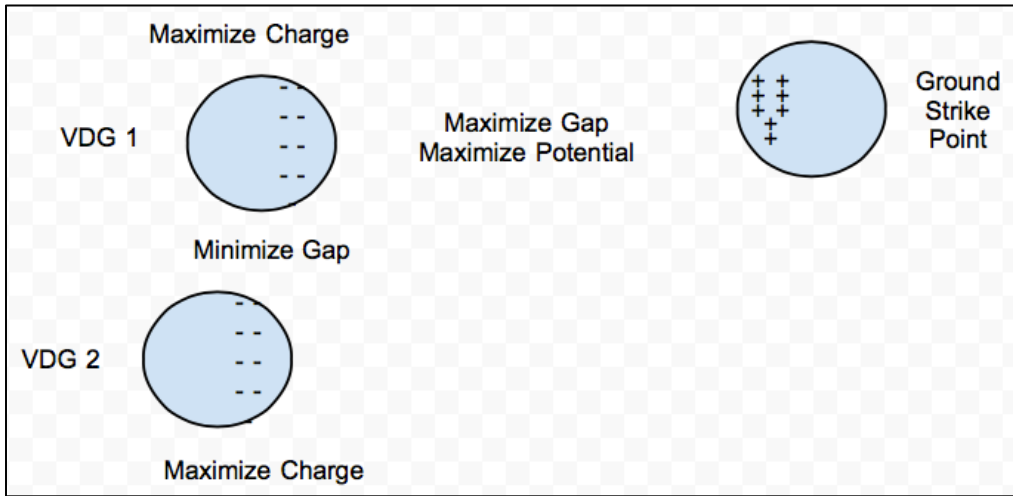


Figure 48. Plan View of Improvement Concept 1.

The second concept proposal is to boost performance by adding a VDG in line as illustrated in Figure 49 and build charge on the VDGs together in parallel. The maximal charge on VDG 1 must be sufficient to overcome the same polarity but minimal charge on VDG 2 and to discharge prior to VDG 2 and through VDG 2 prior to reaching ground. The initially small potential on VDG 2 adds to the ultimate potential but is not initially sufficiently large on its own to ionize the air. Following the discharge of VDG 1, the potential between VDG 2 and ground is theorized to possibly rise instantaneously to be

greater than the breakdown strength of air. Once again, the anticipated and desired end result is to decrease  $t_{100-0}$ .

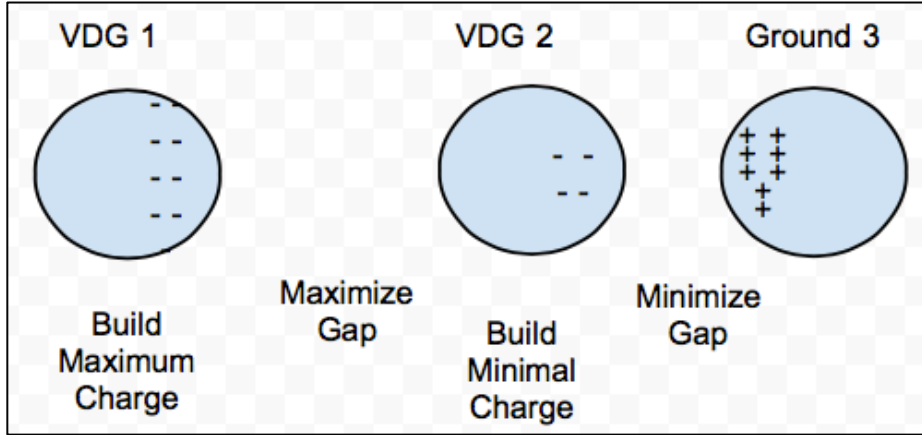


Figure 49. Plan View of Improvement Concept 2

Permutations of the preceding improvement concept proposals are possible and both warrant further consideration.

### Equipment & Facility Improvements

Future research projects will likely require that ringing be further reduced. Future experiments will likely be required to better isolate the desired signal; produce smoother data; and decrease the shot-to-shot variability.

A future project will likely further require the successful use of the D-dot sensor in order to directly analyze the emanating  $E_{EMP}(t)$  rather than to rely on the ground line  $i(t)$  which is adversely affected by the ground line material Z. Optimally, the arcing  $i(t)$  in the air and the  $i(t)$  in the ground line will be fully and independently measured and compared prior to assuming that they are nearly identical. To this end, it is further recommended that a future experiment be executed in a non-reflecting outdoor location. Such a change will

test the assumption that the waves being generated in the current experiment are being reflected off of the laboratory surfaces. In addition to the D-dot sensor and the CVR, a magnetic field sensor and a current probe may also be added to a future design with results compared for additional verifications and to make the research more complete.

A longer range and more optimal improvement will be to perform experiments in a non-reflecting indoor laboratory where the air may be monitored and conditioned. Speculatively, the randomness of the discharge path may be in part due to the environmental variability. Future research will benefit from finding ways to standardize, straighten and increase the consistency of the discharge path to ground.

Future research will also further benefit from considering the findings presented in Table 6 which shows that the measured  $C$  greatly exceeds the calculated  $C$ . The calculation did not consider that capacitances would be significantly increased due to presumed interactions with other components and with the laboratory facility. Recommend that future research include additional consideration of the surrounding structure. Recommend further that a multimeter be routinely available throughout the process to readily check capacitances, inductances, resistances and continuities.

## APPENDIX A: Regression Performed To Fit Equations

With each discharge, a voltage across the CVR was transmitted as a data point to the oscilloscope. Approximately 1200 data points were typically recorded over a 2.4 microsecond duration for each discharge. Each point of voltage data was next divided by the calibrated CVR resistance value of  $0.025 \Omega$  to convert it to a current and all of the actual current values were summed,  $\sum_{j=1}^{j=1200} i_j$ . Next, each current value was squared and then the squares were summed,  $\sum_{j=1}^{j=1200} i_j^2$ . For all 1200 time steps, the known model fit equation  $i_{model}(t) = i_o(e^{-at} - e^{-bt})$  was calculated. Initial values for  $i_o$ ,  $a$ , and  $b$  were guessed. The next values calculated were the sum of the squares due to error,  $SSE$ , the total sum of squares,  $SST$ , and the Goodness of Fit,  $R^2$ .

$$SSE = \sum_{j=1}^{j=1200} (i_{model,j} - i_j)^2$$

$$SST = \left( \sum_{j=1}^{j=1200} i_j^2 \right) - \frac{1}{1200} \left( \sum_{j=1}^{j=1200} i_j \right)^2$$

$$R^2 = 1 - \frac{SSE}{SST}$$

Next, the initial fit values for  $i_o$ ,  $a$ , and  $b$  were all improved using the MS Excel solver tool shown in Figure 50.

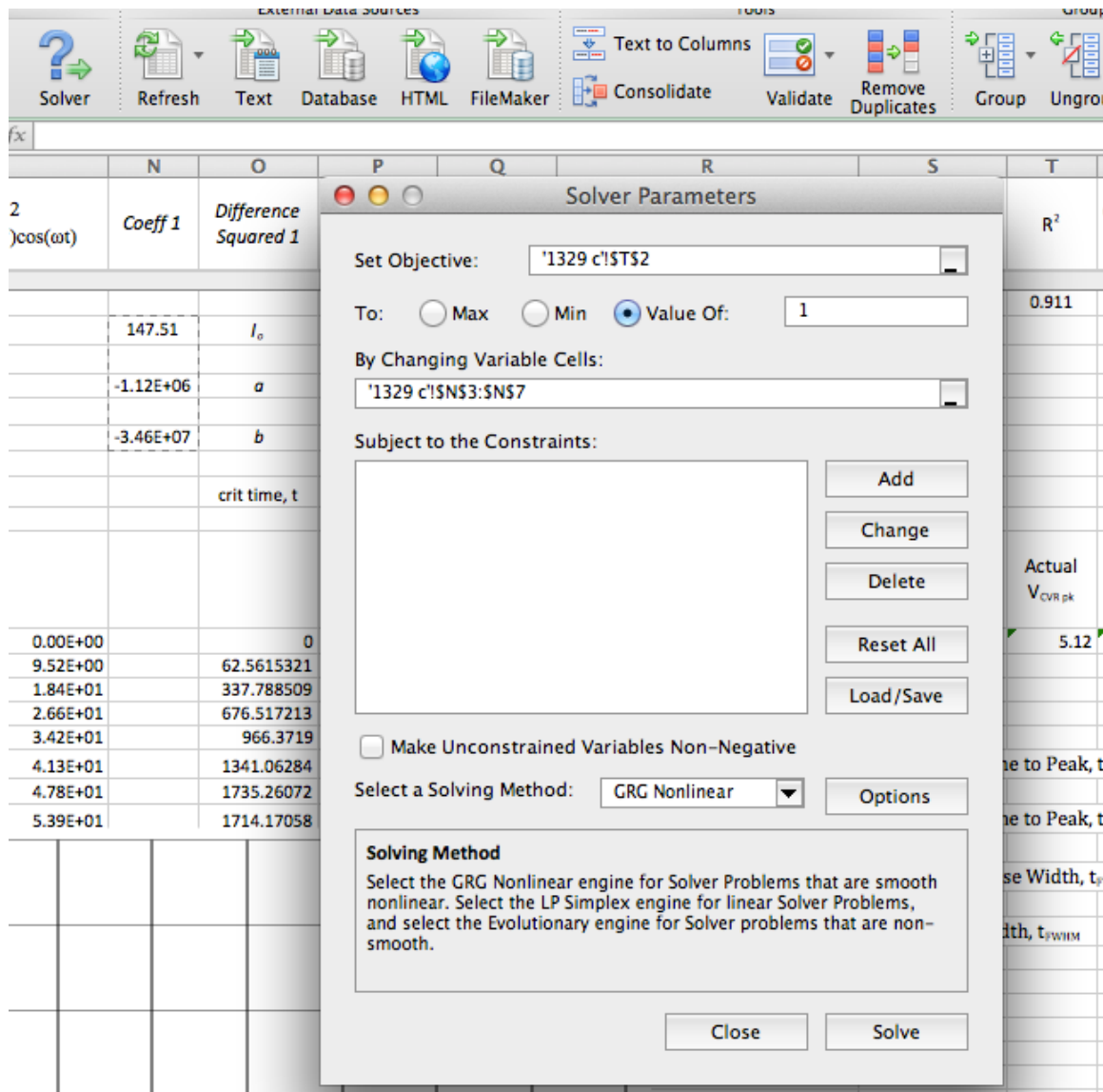


Figure 50. To improve the model fit, the MS Excel solver tool was first selected from the data menu. Next, the  $R^2$  cell is set as the objective cell and the desired objective value is set to unity. The cells holding the constant values  $i_o$ ,  $a$ , and  $b$  of the model are selected for simultaneous processing to minimize SSE; to have  $R^2$  approach unity and to achieve optimal model fit to the actual data.

## Bibliography

- 1) Cook, Gary. Air Force Research Laboratory Scientist John Leahy. 12 July 2013.
- 2) Dishington, R.H., W. R. Hook, and R. P. Hillberg. "Flash lamp Discharge and Laser Efficiency." Applied Optics, 13.10 (1974): 2300-2312.
- 3) Edgel, W. Reed. "Free Field Sensors and Balun" 29 October 2008. Prodyn Technologies.
- 4) Edgel, W. Reed. "Primer on Electromagnetic Field Measurements." 29 October 2008. Prodyn Technologies.
- 5) Gabrielson, B.C., The Aerospace Engineers Handbook of Lightning Protection, Don White Publishing, Gainesville, VA, 1986.
- 6) Johnson, Gary L. "Tesla Coil Impedance." The First Tesla Museum and Science Center International Conference on Nikola Tesla. Farmingville, New York: 2006. Ch 2, pg 7.
- 7) Knoll, Glenn F. Radiation Detection and Measurement. 3. Ann Arbor, MI: John Wiley and Sons, Inc, 2000.
- 8) Kodali, Prasad V., Engineering Electromagnetic Compatibility, Second Edition, IEEE , Inc. New York, 2001.
- 9) Markiewicz, J.P., and J.L. Emmett. "Design of Flash lamp Driving Circuits." IEEE Journal of Quantum Electronics, 2.11 (1966): 707-711.
- 10) Paul, Clayton R. Introduction to Electromagnetic Compatibility. 2. Hoboken, NJ: John Wiley and Sons, Inc, 2006.

- 11) Serway, Raymond A. Physics for Scientists and Engineers. 7. Belmont: Thomson Higher Education, 2008.
- 12) T & M Research Products. SERIES SDN-414 Current Viewing Resistors Description. 6 April 2011.
- 13) US Air Force Aeronautical Systems Center. "Electromagnetic Environmental Effects Requirements for Systems Military Standard 464." Department of Defense Interface Standard. Wright Patterson AFB: US Department of Defense, 18 March 1997.

<b>REPORT DOCUMENTATION PAGE</b>				<i>Form Approved OMB No. 074-0188</i>
<p>The public reporting burden for this collection of information is estimated to average 1 hour per response, including the time for reviewing instructions, searching existing data sources, gathering and maintaining the data needed, and completing and reviewing the collection of information. Send comments regarding this burden estimate or any other aspect of the collection of information, including suggestions for reducing this burden to Department of Defense, Washington Headquarters Services, Directorate for Information Operations and Reports (0704-0188), 1215 Jefferson Davis Highway, Suite 1204, Arlington, VA 22202-4302. Respondents should be aware that notwithstanding any other provision of law, no person shall be subject to an penalty for failing to comply with a collection of information if it does not display a currently valid OMB control number.</p> <p><b>PLEASE DO NOT RETURN YOUR FORM TO THE ABOVE ADDRESS.</b></p>				
1. REPORT DATE (DD-MM-YYYY) 11-08-2016		2. REPORT TYPE Master's Thesis		3. DATES COVERED (From – To) October 2010 – August 2016
TITLE AND SUBTITLE  Experimental Testing Of A Van De Graaff Generator As An Electromagnetic Pulse Generator			5a. CONTRACT NUMBER	
			5b. GRANT NUMBER	
			5c. PROGRAM ELEMENT NUMBER	
6. AUTHOR(S)  John S. Leahy, Lieutenant Colonel, USA			5d. PROJECT NUMBER	
			5e. TASK NUMBER	
			5f. WORK UNIT NUMBER	
7. PERFORMING ORGANIZATION NAMES(S) AND ADDRESS(S) Air Force Institute of Technology Graduate School of Engineering and Management (AFIT/ENY) 2950 Hobson Way, Building 640 WPAFB OH 45433-8865			8. PERFORMING ORGANIZATION REPORT NUMBER AFIT-ENP-MS-16-S-075	
9. SPONSORING/MONITORING AGENCY NAME(S) AND ADDRESS(ES) Air Force Nuclear Weapons Center 8601 Frost Ave, SE Kirtland AFB, NM 87117 ATTN: Cynthia Herrera			10. SPONSOR/MONITOR'S ACRONYM(S) AFNWC	
			11. SPONSOR/MONITOR'S REPORT NUMBER(S)	
12. DISTRIBUTION/AVAILABILITY STATEMENT DISTRUBUTION STATEMENT A. APPROVED FOR PUBLIC RELEASE; DISTRIBUTION UNLIMITED.				
13. SUPPLEMENTARY NOTES This material is declared a work of the U.S. Government and is not subject to copyright protection in the United States.				
14. ABSTRACT The purpose of this research was to evaluate an existing Van de Graaff generator facility for use as an EMP research tool. In order to assess the Van de Graaff, the unclassified Military Standard 464, which specifies a testing free field wave as having an intensity of 50 kV/m with a time-to-peak, of no more than 5 ns, was used as a baseline for free field analysis and this temporal standard used as a basis for generated currents. Unfortunately, the free field measurements were subject to substantial electronic interference from electromagnetic coupling from internal wall reflections, invalidating the assessment. Therefore the primary research focus was to replicate the temporal character of the current through the Van De Graaff, which would represent the most direct coupling that could be expected from a free field wave. The research indicated that the generated time-to-peak (a.k.a rise time) is an order of magnitude greater than that of the Military Standard 464. The fall time is much faster than specified in Military Standard 464 due to substantial ringing in the line. Proposed improvements to the VDG system are described in this thesis.				
15. SUBJECT TERMS Electromagnetic Pulse, Van De Graaff, Electromagnetic Coupling				
16. SECURITY CLASSIFICATION OF:		17. LIMITATION OF ABSTRACT UU	18. NUMBER OF PAGES 91	19a. NAME OF RESPONSIBLE PERSON James C. Petrosky, AFIT/ENP
a. REPORT U	b. ABSTRACT U	c. THIS PAGE U		19b. TELEPHONE NUMBER (Include area code) (937) 255-6565, ext 4562 (james.petrosky@afit.edu)

Standard Form 298 (Rev. 8-98)  
Prescribed by ANSI Std. Z39-18